

A Study of the Ignition Mechanism for Dead Pinus Palustris Needles

by
Weixuan Gong



A Thesis
Submitted to the Faculty
Of the
WORCESTER POLYTECHNIC INSTITUTE
In partial fulfillment of the requirements for the
Degree of Master of Science
in
Fire Protection Engineering

January 2023

APPROVED:

Prof. Albert Simeoni, Major Advisor, FPE Department, WPI

Prof. James Urban, Co-Advisor, FPE Department, WPI

Abstract

Combinations of cumulative impacts of drought, invasive species, climate variability, and ever-expanding wildland-urban interface make landscapes more susceptible to devastating wildland fires. To treat the increasing risks of wildland fires, one of the best ways is to prevent them from happening, which requires a solid understanding of the mechanisms driving the ignition of vegetation fuels. This can be achieved mainly through describing the pyrolysis and the ignition processes.

For the pyrolysis process of vegetation fuels, there is a shortage of studies on the dynamic chemical evolution of pyrolysis gases. Concerning the ignition process, it is not clear how the critical mass loss rate and the heat release rate per unit area at ignition are influenced by different external conditions.

Motivated by these challenges, two series of experiments were conducted using a modified cone calorimeter to understand the mechanisms driving the ignition of dead *Pinus palustris* needles. In the first set of experiments, Fourier-transform infrared spectroscopy (FTIR) was used to dynamically characterize the composition of the pyrolysis gases generated from the thermal degradation of pine needles exposed to various incident heat fluxes (20 and 30 kW/m²), and a nitrogen inflow of 50 l/min. In the second set of experiments, the ignition of pine needles was studied for varied incident heat fluxes (20 to 35 kW/m²) and air flow rates (buoyancy-induced, 50 and 100 l/min forced flow).

The results of the first series of experiments showed that methane (CH_4), carbon monoxide (CO), carbon dioxide (CO_2), and water vapor (H_2O) were the main constituents of the pyrolysis gases. The predominance of these compounds was found to be independent of the external heat flux, while their concentrations were sensitive to it. The heat of combustion of the pyrolysis gas and the pyrolysis reaction rate were found to increase with increasing external heat fluxes. The results from the second series of experiments showed that the critical mass loss rate at ignition increased with both flow rates and heat flux, while the heat release rate per unit area at ignition was only significantly influenced by the flow

conditions. The analysis of the results suggests a significant contribution of smoldering combustion to the flaming ignition under low heat fluxes and high airflow rate conditions.

Key words: Wildfire ignition, Pyrolysis gas evolution, FTIR spectrometry, Modified cone calorimeter

Acknowledgments

I am very grateful to Dr. Juan Cuevas for his guidance and helping me revise this thesis over the whole year. I would also like to thank Prof. Albert Simeoni for his encouragement and guidance over the last two years, and Prof. James Urban for his suggestions for analyzing and presenting the results of the experiments.

I must express my gratitude to the lab staff, Russell G. Lang, Brokaw Frederick, and Raymond Ranellone for their assistance with assembling the experimental set-up and training me on the use of the lab equipment.

I also appreciate the care and support from Ms. Poirier and my friends: Abhi, Navya, Luke, and Jon.

Table of Contents

ABSTRACT	I
ACKNOWLEDGMENTS	III
TABLE OF CONTENTS	IV
NOMENCLATURE	VI
LIST OF FIGURES	VIII
LIST OF TABLES	IX
CHAPTER 1. INTRODUCTION	1
1.1 Background	1
1.2 Description of the Ignition Process	1
1.3 Work of This Thesis	3
1.4 A Brief Summary of This Thesis	3
1.5 References	5
CHAPTER 2. LITERATURE REVIEW AND THESIS OBJECTIVE	6
2.1 Literature Review	6
2.2 Research Gaps in Piloted Ignition	10
2.3 Objectives of This Thesis	10
2.4 References	11
CHAPTER 3. EXPERIMENTAL METHODOLOGY	14
3.1 Experimental set-up	14
3.2 Sample preparation	17
3.3 Experimental methods	18
3.4 References	27

CHAPTER 4. RESULTS AND DISCUSSION	28
4.1 Pyrolysis test	28
4.2 Ignition tests	32
4.3 References	41
CHAPTER 5. CONCLUSION AND FUTURE WORK	42
5.1 Conclusion	42
5.2 Future work	42
APPENDIX A. UNCERTAINTY ANALYSIS OF HEAT OF COMBUSTION EVALUATION	44

Nomenclature

ABS	Absolute function
c	Specific heat (J/kg-K)
CC	Cone calorimeter
CCP	The product of concentration and pathlength of an FTIR spectrum (ppm-m)
E	Activation energy
FMC	Fuel moisture content (%)
fps	Frames per second
FTIR	Fourier transform infrared
H _c	Heat of combustion (kJ/g)
HRR	Heat release rate (kW)
HRRPUA	Heat release rate per unit area at ignition (kW/m^2)
k	Thermal conductivity (kW/m-K)
L	Absorption pathlength (m)
LOD	Limit of detection (ppm)
m	Mass (g)
M	Molecular weight (g/mol)
\dot{m}	Mass loss rate (g/s)
MIL	Minimum instrumental linewidth (cm^{-1})
MLRPUA	Mass loss rate per unit area at ignition (g/m^2s)
P	Pressure (Pa)
\dot{Q}	Heat release rate (kW)
R	Ideal gas constant (J/mol-K)
RSA	Residual squared area ($abs - cm^{-1}$)
RWA	Wavenumber accuracy (cm^{-1})
T	Temperature ($^{\circ}C$ or K)
tig	Time to ignition (s)
w	Wavenumber
X	Mole fraction
Y	Mass fraction

Greek symbols

ρ	Density (kg/m^3)
ω	Reaction rate
σ	Standard deviation

Subscripts

ad	After oven-drying
amb	Ambient
bd	Before oven-drying
ch	Chemical
cor	Correction
cr	Critical
f	Flame
ig	At ignition
p	Lower limit of a wavenumber range
pyr	Pyrolysis
q	Upper limit of a wavenumber range
R	Reference spectrum
S	Sample spectrum
smold	Smoldering

Superscripts

"	Per unit area
0	Initial

List of Figures

Figure 1.1 Schematic of the process occurring as a solid material undergoes heating before ignition induced by an external energy source [6].....	2
Figure 3.1 Schematic of the cone calorimeter for its original design [13].....	14
Figure 3.2 Experimental apparatus: modified cone calorimeter allowing for gas inflow through the sample and pyrolysis gas measurement.	15
Figure 3.3 Fuel samples for the tests with (a) buoyancy-induced flow using the basket of 0% opening and (b) forced flow using the basket of 63% opening	18
Figure 3.4 Cone heater heat flux calibration	19
Figure 3.5 Reference spectra for CH ₄ , CO, CO ₂ , and H ₂ O from the EPA spectra database [7]	23
Figure 4.1 Pyrolysis gas FTIR spectra at 50 l/min N ₂ and (a) 20 kW/m ² , 50 l/min N ₂ and (b) 30 kW/m ²	29
Figure 4.2 Pyrolysis gas volume concentration evolution at (a) 20 kW/m ² , 50 l/min N ₂ and (b) 30 kW/m ² , 50 l/min N ₂ . The concentrations of each gas species at t _{ig} were determined by combining the observed time-to-ignition values in the ignition tests (See section 4.2).	30
Figure 4.3 Flame location at ignition captured for heat flux ranging from 25 to 35 kW/m ² with air flow rates from 0 to 100 L/min.	32
Figure 4.4 Mean ignition time (t _{ig}) for heat flux ranging from 20 to 35 kW/m ² with air flow rates from 0 to 100 L/min	33
Figure 4.5 Mass loss rate per unit area for sustained flaming ignition (MLRPUA _{ig}). MLRPUA _{pyr} was determined by combining the observed time-to-ignition values in the ignition tests with the mass loss rate measured from the pyrolysis tests.	35
Figure 4.6 Heat Release Rate per unit area at ignition (HRRPUA _{ig}) for sustained flaming ignition	37
Figure 4.7 Selected control volume (outlined by the red dashed rectangle) for the energy balance analysis at flaming ignition	38
Figure 4.8 Mass loss rate evolution (MLR) for tests conducted with (a) 20 kW/m ² , 50 l/min N ₂ and O ₂ , and (b) 30 kW/m ² , 50 l/min N ₂ and O ₂	40

List of Tables

Table 3.1 Fuel properties.....	17
Table 3.2 FTIR spectrometer system configuration.....	21
Table 3.3 RSA and LOD analysis for target pyrolysis constituents.....	23
Table 3.4 RWA check for the FTIR system configuration	24
Table 3.5 Pyrolysis test procedure	25
Table 3.6 Ignition test procedure.....	26
Table 3.7 Experimental matrix.....	26
Table 4.1 Average concentration of each gas component in the pyrolysis gas.....	31
Table 4.2 Concentration of each gas component at ignition	31
Table 4.3 Energy provided to the ignition by pyrolysis gas combustion and smoldering combustion for 20 and 30 kW/m ² under 50 l/min ambient air	40

Chapter 1. INTRODUCTION

1.1 Background

There is an increasing risk of destructive wildland fires due to changing ecology as well as increased intermingling between human activities and undeveloped wildland. Combinations of cumulative impacts of drought, invasive species, climate variability [1], and the constant expansion of the wildland-urban interface make landscapes more susceptible to devastating fires.

To reduce the loss from the result of wildfire, actions that can be taken include ignition prevention, vegetation fuel management, suppression response, and home ignition zone management [2]. Among these methods, one of the best ways to mitigate the risk of wildfire is to avoid unwanted ignitions, which requires a solid understanding of the ignition of vegetation fuels.

In terms of ignition sources, wildland fires often occur with a pilot source where the flaming ignition is initiated by a localized energy supply to a mixture of gasified fuel and oxidizer. From reported cases, most wildland fires are caused by lighting, inappropriate fire use, smoking, and arson [3].

Therefore, to conduct a study that is representative of wildland fires, the topic of this thesis is the piloted flaming ignition of vegetation fuel.

1.2 Description of the Ignition Process

The piloted flaming ignition of the solid refers to the ignition of the fuel vapors driven off from the solid at the location of the pilot source. Thus, the key parameters controlling the occurrence of ignition are the concentration of fuel vapors released by pyrolysis, oxygen availability, and temperature.

The pyrolysis process depends on the heat transfer in the solid phase for its decomposition [4], while it controls the amount of generated fuel vapor. Once exposed to an external heating source, the temperature of a solid will start to increase in depth, as shown in Figure 1.1. The temperature rise and distribution are mainly controlled by the material properties of the solid, which include the density (ρ), the thermal conductivity (k), and the specific heat (c). For vegetation fuels, the spatial structure (e.g.,

porosity) also influences the heat transfer inside the solid. After the surface temperature of the solid reaches the pyrolysis temperature, the solid fuel degrades and producing significant gaseous fuel and product gases. The generation rate of the fuel vapor also referred to as the pyrolysis rate, is commonly described by Arrhenius-type functions, as shown in Eq (1.1) [5]. From the equation, a rise in temperature increases the rate of pyrolysis.

$$\dot{\omega} = Ae^{-\frac{E}{RT}}f(\alpha) \quad \text{Eq (1.1)}$$

where $\dot{\omega}$ is the reaction rate, A is the pre-exponential factor; E is the activation energy; R is the ideal gas constant; T is the solid fuel temperature; and $f(\alpha)$ is the kinetic reaction mechanism.

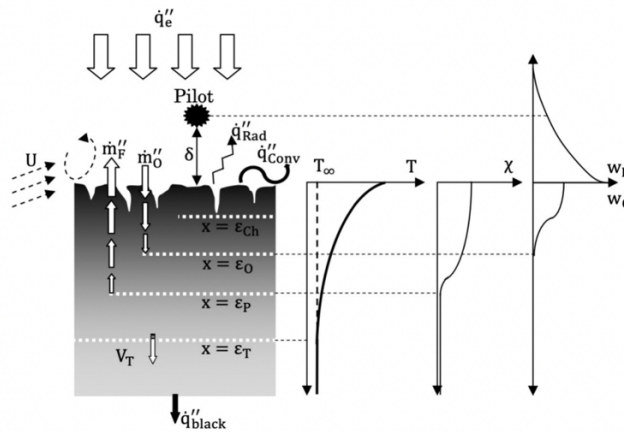


Figure 1.1 Schematic of the process occurring as a solid material undergoes heating before ignition induced by an external energy source [6]

The influence of the fuel properties on the pyrolysis rate is implicitly indicated by E in Eq (1.1). For example, Liu et al. [7] reported values of E for different temperature ranges during the decomposition of a total of 16 plant species and found that E varies with the species.

After pyrolysis occurs, a sufficient concentration of fuel vapor and energy is required for ignition to occur [8].

The concentration of the fuel vapor generated from pyrolysis is required to be within the flammability limit, which depends on the given mixture of fuel vapor and air, to achieve the ignition conditions [8]. The generated fuel vapor from the pyrolysis process for vegetations mainly consists of CH_4 , CO , CO_2 , and H_2O [9, 10] and the amount of each gas product is influenced by the plant species [10] and

the pyrolysis temperature [11], and the availability of oxygen [12]. The air also influences the flammability of the resulting pyrolysate fuel and air mixture in terms of its velocity field and oxygen concentration [13, 14]. Therefore, the flammability limit of the fuel-air mixture is a function of the fuel properties, the pyrolysis temperature, the air velocity field, and the oxygen concentration.

Finally, having the fuel-air mixture within the flammability limit, ignition is initiated with a pilot source, which can be a flame, a spark, or a hot spot that is capable of providing a high temperature to achieve the ignition [15].

1.3 Work of This Thesis

The aim of this thesis is mainly to investigate the mechanisms driving the ignition of *Pinus palustris* needles under different flow, external heating, and oxygen concentration. Based on the ignition description in section 1.2, the focus of this work is on understanding and describing how the pyrolysis process and the ignition of the fuel vapor from pyrolysis are influenced by different heating fluxes of and air flow rates.

1.4 A Brief Summary of This Thesis

Chapter 2 starts with a brief literature review of pyrolysis and the occurrence of the ignition of the solid (section 2.1). Then, certain gaps are listed according to the literature (section 2.2). Finally, driven by the existing gaps, two main objectives of this thesis are identified (section 2.3). The first objective is to characterize the pyrolysis process of dead *Pinus palustris* needles by modifying the setup of the cone calorimeter and adding FTIR Spectroscopy. The second objective is to characterize the ignition process of the same fuel using the modified cone calorimeter.

Chapter 3 first introduces the design of the experimental set-up (section 3.1). The modifications made from the original design of the cone calorimeter and the connection of the FTIR spectrometer to the modified cone calorimeter are introduced in detail. Then, the fuel properties, obtained after drying the fuel

in an oven are estimated (section 3.2). Lastly, the experimental method is described in detail, including the apparatus calibration, test design matrix and test procedures (section 3.3).

Chapter 4 presents the analysis of the experimental results. The whole analysis is divided into two parts based on the two types of tests that have been conducted. The first part (section 4.1, corresponding to the pyrolysis tests) is the analysis of the pyrolysis process. The influence of varying external heat fluxes on the evolution of the pyrolysis gas is investigated. The second part (section 4.2, corresponding to the ignition tests) is the analysis of the ignition process. The influences of varying external heat fluxes and airflow rates on the position of the flame at ignition, time-to-ignition, the critical mass loss rate, and the heat release rate per unit area are discussed.

Chapter 5 presents the conclusions on the results from Chapter 4 for the pyrolysis and the ignition tests, respectively and points out the potential of quantifying the smoldering contributions to the flaming ignition at the bench-scale (section 5.1). Then, future work in which the primary aim is to better understand the role of smoldering on the flaming ignition is briefly discussed (section 5.2).

1.5 References

- [1] H. B. Richer *et al.*, “Probing the faintest stars in a globular star cluster,” *Science* (1979), vol. 313, no. 5789, pp. 936–940, Aug. 2006, doi: 10.1126/science.1130691.
- [2] D. E. Calkin, J. D. Cohen, M. A. Finney, and M. P. Thompson, “How risk management can prevent future wildfire disasters in the wildland-urban interface,” *Proc Natl Acad Sci U S A*, vol. 111, no. 2, pp. 746–751, 2014, doi: 10.1073/pnas.1315088111.
- [3] J. P. Prestemon *et al.*, “Wildfire Ignitions: A Review of the Science and Recommendations for Empirical Modeling A Conceptual Model of Wildfire Ignitions and Prevention Wildfire Ignitions Processes and Prevention Activity Effectiveness Wildfire Cause Variables Predicting Wildfire Ignitions Spatial and Temporal Ignition Patterns and Trends Recommendations for Modeling of Wildfire Ignitions and Prevention.” [Online]. Available: www.srs.fs.usda.gov
- [4] T. Rogaume, “Thermal decomposition and pyrolysis of solid fuels: Objectives, challenges and modelling,” *Fire Safety Journal*, vol. 106. Elsevier Ltd, pp. 177–188, Jun. 01, 2019. doi: 10.1016/j.firesaf.2019.04.016.
- [5] H. E. Kissinger, “Reaction Kinetics in Differential Thermal Analysis,” *Analytical Chemistry*, vol. 29, no. 11, pp. 1702–1706, Nov. 1957, doi: 10.1021/ac60131a045.
- [6] N. Bal, “Uncertainty and complexity in pyrolysis modelling,” postgraduate dissertation, the University of Edinburgh, Aug. 2012. <https://www.researchgate.net/publication/292611832>
- [7] N. A. Liu, W. Fan, R. Dobashi, and L. Huang, “Kinetic modeling of thermal decomposition of natural cellulosic materials in air atmosphere,” *Journal of Analytical and Applied Pyrolysis*, vol.63, no.2, pp:323-325,2002. www.elsevier.com/locate/jaap
- [8] J. G. Quintiere, *Fundamentals of fire phenomena*. John Wiley, 2006.
- [9] F. Shafizadeh, “Introduction to pyrolysis of biomass,” *Journal of Analytical and Applied Pyrolysis*, vol. 3, pp. 283-305, 1982.
- [10] E. Amini, M. S. Safdari, J. T. DeYoung, D. R. Weise, and T. H. Fletcher, “Characterization of pyrolysis products from slow pyrolysis of live and dead vegetation native to the southern United States,” *Fuel*, vol. 235, pp. 1475–1491, Jan. 2019, doi: 10.1016/j.fuel.2018.08.112.
- [11] M. I. Jahirul, M. G. Rasul, A. A. Chowdhury, and N. Ashwath, “Biofuels production through biomass pyrolysis- A technological review,” *Energies*, vol. 5, no. 12. MDPI AG, pp. 4952–5001, 2012. doi: 10.3390/en5124952.
- [12] C. Lautenberger and C. Fernandez-Pello, “A model for the oxidative pyrolysis of wood,” *Combust Flame*, vol. 156, no. 8, pp. 1503–1513, Aug. 2009, doi: 10.1016/j.combustflame.2009.04.001.
- [12] T. Ma, “A thermal theory for estimating the flammability limits of a mixture,” *Fire Safety Journal*, vol. 46, no. 8, pp. 558–567, Nov. 2011, doi: 10.1016/j.firesaf.2011.09.002.
- [13] D. Gardiner, M. Bardon, and G. Pucher, “An Experimental and Modeling Study of the Flammability of Fuel Tank Headspace Vapors from High Ethanol Content Fuels,” 2008. [Online]. Available: <http://www.osti.gov/bridge>
- [14] N. Kawahara, S. Hashimoto, and E. Tomita, “Plasma temperature of spark discharge in a spark-ignition engine using a time series of spectra measurements,” 2016.

Chapter 2. LITERATURE REVIEW AND THESIS OBJECTIVE

2.1 Literature Review

In this section, a brief review of the ignition of solid fuels is presented through heating, pyrolysis, and the occurrence of flaming ignition.

2.1.1 Heating

In this work, the heating stage refers to the time during which the solid fuel is exposed to an external heating source before pyrolysis occurs. The temperature rise and distribution inside the fuel are influenced by its material properties which include density (ρ), thermal conductivity (k), and specific heat (c). However, it is difficult to measure these properties for thin biological fuels because the measurement of thermal properties such as k and c involves heating the sample, which leads to changes in properties and damage [1]. For example, Liu et al. [2] reported that the mass loss of a vegetative fuel sample was about 10% during the heating phase, due to evaporation of water prior to pyrolysis. Also, the heating process also causes the shrinkage of vegetation fuels, such as leaves [3]. To avoid large temperature rises inside the solid fuel, which may change the material properties, the photothermal technique has been developed to determine the values of k and c where the temperature rise is negligible (only a few mK) inside the solid fuel during the measurement [4]. Briseño-Tepepa et al. [5] successfully applied this technique to measure the thermal properties of plant leaves.

2.1.2 The pyrolysis process

To describe the pyrolysis process of a solid, it is necessary to characterize both the kinetic of thermal decomposition for the solid and the chemical evolutions with respect to atmosphere and temperature [6].

The mode of thermal decomposition, which is a function of temperature, oxygen availability, and kinetic parameters, has been explored by abundant studies [7-14]. There are three primary approaches to studying the thermal decomposition: (1) modeling, (2) the free-model method, and (3) the hybrid approach. The modeling method, in general, requires identifications of a reaction mechanism, a kinetic

law (usually in an Arrhenius form), and a function of conversion. Liu et al. [15] developed a kinetic thermal decomposition modeling for eight species of biofuels. This paper first identified a three-step reaction mechanism by DTG investigation on mass loss and mass-loss rate, then assumed a modified Arrhenius relationship as a representation for mass loss kinetics and found the first-order reaction fit best the proposed model. Kinetic parameters, "E" and "A" were extracted from the best fitting curve. This model was verified by reconstructing the mass loss data for each species.

As shown in [16,17] using the model-free approach experimentally derived the values for "E" and "A" using a differential thermal analysis (DTA) for mineral materials. The principle behind this approach is that the peak temperature shown on the DTA curve is the temperature corresponding to the maximum reaction rate. Meanwhile, the limit of this model-free method is the applicability only for one-reaction decomposition or fully separated reactions.

The University of Corsica conducted a more advanced thermal decomposition studies on Mediterranean shrub species [18]. The authors exercised a hybrid approach to establish the decomposition modeling with experimentally developed kinetic parameters. Despite the attainment of a good match between the modeling and these micro-scale experimental results, great care should be taken here is the suitability of the Arrhenius law on describing the mass loss kinetics, which takes place in the condensed phase. Furthermore, scaling-up experiments are vital to decoding the decomposition mechanism beyond the microscale level in real cases. However, issues arise when scaling up the experiments due to the difficulty of controlling the boundary conditions and of obtaining accurate material properties for each reaction step. Despite the good match between the experimental results and the models developed by the literature mentioned above, the suitability of the Arrhenius type equation to the decomposition of the solid needs to be checked [19, 20].

Unlike the thermal decomposition mode, the chemical evolutions of the pyrolysis process received less attention and there are only a few studies available that investigated it. In terms of the pyrolysis products that mainly include the tar, char, and light gases, [21-23] studied the influences of the temperature on their yields; it also measured the average concentration of each component in the

pyrolysis gas for the plant biomass with FTIR spectroscopy. Ningbo et al. [24] investigated the effects of heating temperature and solid residence time on the average concentration of each constituent in the pyrolysis gas of pine sawdust with a gas chromatograph. However, despite a good identification of the pyrolysis gases by these studies, there is a lack of focus on the dynamic evolution of the pyrolysis gas components. Consequently, it is challenging to quantify the flammability [25] of the fuel vapor-air mixture in the gas phase where combustion occurs.

2.1.3 The occurrence of flaming ignition

The occurrence of flaming ignition can be identified when a sustained flame is observed based on test standards [26, 27]. However, few studies reported the position of the observed flame at the ignition. Kwon et al. [28] recorded the flame onset and its propagation for PMMA using a high-speed camera with 250 fps and found that the ignition points occur in the gas phase but could migrate away from the radiation heater as the heating source temperature increases. Nakamura and Kashiwagi [29] simulated the non-piloted ignition of methylmethacrylate and showed the ignition always occurs in the gas phase.

Besides the visual observation, two criteria define the ignition occurrence [23]: one for the gas phase and the other for the condensed phase. For the gas-phase ignition criterion, the minimum fuel/air ratio, which supports the combustion reaction, must be determined at the pilot location. The criterion was rarely applied because of the difficulty of quantifying the corresponding flow field [30].

The condensed-phase criteria,[16], including ignition temperature (T_{ig}) [31], critical mass loss rate (MLR_{cr}) [32, 33], and heat release rate at ignition (HRR_{ig}) [32], are more likely to be measured and thus more frequently used. Moreover, all of these criteria should combine material properties and specific environmental conditions [34].

T_{ig} , the most common piloted ignition criterion in engineering modeling and calculations, is a function of material properties, incident heat flux level, solid initial temperature, and experimental conditions. Li et al. [35] evaluated T_{ig} values for biomass fuels through the peak of corresponding TGA curves and found it varies with fuel moisture content and particle size. Cordova et al. [36] measured

ignition temperature for PMMA samples using the LIFT apparatus and reported T_{ig} would increase with heat flux levels and flow velocities. Besides the actual measurements, the value of T_{ig} can also be identified with a simple theoretical model [37] based on the measurements of the minimum heat flux for ignition, whose value can be obtained more easily. However, the validity of this derived T_{ig} needs to be checked before it is put into the model for predicting the ignition due to the assumption that the solid is treated as inert [38] before ignition. Therefore, the derived critical surface temperature may not be suitably selected as an ignition criterion for materials that can undergo smoldering prior to ignition. For example, the experimental measurements of T_{ig} for wood range from 250 ~ 400 °C [39].

The piloted ignition can also be predicted by a critical mass flow, \dot{m}''_{cr} , of volatiles, which is a function of ambient temperature, test conditions, and material properties. Lyon and Quintiere [32] considered critical mass flow rate as a good predictor for transient and sustained ignition of combustible polymers and found that fuel vapor's critical mass flow rate for sustained ignition is about three times greater than that for transient ignition given free convection conditions. A potential explanation is that there is a transition from burning at the lean flammability limit for the flash point to burning at stoichiometric conditions for the fire point. Mcallister et al. [40] reported that the critical mass flux at flaming ignition is positively correlated to the moisture content and external heat flux for woody materials. The dependence of O_2 concentration on the critical fuel mass flux was reported by [26] and [34]. Rich et al. [42] reported the influence of material properties, flow velocity, and oxygen concentration on the critical mass loss rate.

As another ignition indicator, the heat release rate per unit area at ignition can then be derived from the critical mass flux. Unlike the critical fuel mass flux at ignition, the heat release rate at ignition is independent of material properties as it implies the minimum energy that can support a flame, but its value is still subject to ambient temperature and convection rates [32].

However, the suitability of these criteria needs to be checked and verified because it has not been verified over the broad ranges reported in the literature mentioned above.

2.2 Research Gaps in Piloted Ignition

As reviewed in Section 2.1, despite the abundance of studies on piloted solid ignition, gaps exist when describing both the pyrolysis process and the occurrence of the flaming ignition. For the pyrolysis process, it is essential to scale up the experiments with properly controlled boundary conditions from the micro-scale experiments (e.g. TGA and DSC studies) to investigate the kinetics of the mass loss (the thermal decomposition of the solid fuel) more like the real cases. Meanwhile, it is necessary to investigate the dynamic chemical evolution of the pyrolysis process together with the thermal decomposition of the solid to fully explain the pyrolysis process of the solid.

Regarding the occurrence of flaming ignition, the relative positions of the flame with respect to the pilot source should be reported to better understand the gas-phase ignition. The solid-phase ignition criteria, specifically the critical fuel mass flux and the heat release rate per unit area at ignition, should also be investigated for different test conditions (e.g., convection rates) and various fuels.

2.3 Objectives of This Thesis

Motivated by the current technique and the challenges, based on the focus of the thesis (mentioned in 1.3), the objectives of this work are dual.

The first objective is to explore the influence of the external heat flux on the pyrolysis process of dead *Pinus palustris* needles by connecting an FTIR spectrometer to a modified cone calorimeter. The pyrolysis gas evolution is expected to be characterized and quantified by FTIR spectroscopy. Meanwhile, the mass evolution of the fuel bed in the pyrolysis process is recorded.

The second objective is to investigate the influence of different experimental conditions on the two solid-phase ignition criteria (critical mass loss rate and heat release rate per unit area at ignition) for porous pine needle beds using the same modified cone calorimeter. Measurements include the time-to-ignition, the flame position at ignition, the critical mass loss rate, and the heat release rate per unit area at ignition (see Chapter 3).

2.4 References

- [1] M. S. Jayalakshmy and J. Philip, "Thermophysical properties of plant leaves and their influence on the environment temperature," *International Journal of Thermophysics*, vol. 31, no. 11–12, pp. 2295–2304, Dec. 2010, doi: 10.1007/s10765-010-0877-7.
- [2] N. A. Liu, W. Fan, R. Dobashi, and L. Huang, "Kinetic modeling of thermal decomposition of natural cellulosic materials in air atmosphere," *Journal of Analytical and Applied Pyrolysis*, vol. 63, no. 2, pp. 323–325, 2002. www.elsevier.com/locate/jaap
- [3] S. Essaghi, M. Hachmi, M. Yessef, and M. Dehhaoui, "Leaf shrinkage: a predictive indicator of the potential variation of the surface area-to-volume ratio according to the leaf moisture content," *Springerplus*, vol. 5, no. 1, Dec. 2016, doi: 10.1186/s40064-016-2900-3.
- [4] C. P. Menon, and J. Philip, "Simultaneous determination of thermal conductivity and heat capacity near solid state phase transitions by a photopyroelectric technique," 2000. *Measurement Science and Technology*, vol. 11, no. 12. <https://iopscience.iop.org/article/10.1088/0957-0233/11/12/314>
- [5] B. R. Briseño-Tepepa, J. L. Jiménez-Peréz, R. Saavedra, R. González-Ballesteros, E. Suaste, and A. Cruz-Orea, "Photopyroelectric microscopy of plant leaves," *International Journal of Thermophysics*, vol. 29, no. 6, pp. 2200–2205, Dec. 2008, doi: 10.1007/s10765-007-0262-3.
- [6] V. Leroy, E. Leoni, and D. Cancellieri, "Thermal Degradation of Lignocellulosic Fuels: Biopolymers Contribution," in *Biopolymers*, Sciyo, 2010. doi: 10.5772/10267.
- [7] S. I. Stoliarov, F. Raffan-Montoya, R. N. Walters, and R. E. Lyon, "Measurement of the global kinetics of combustion for gaseous pyrolyzates of polymeric solids containing flame retardants," *Combustion and Flame*, vol. 173, pp. 65–76, Nov. 2016, doi: 10.1016/j.combustflame.2016.08.006.
- [8] J. D. Swann, Y. Ding, and S. I. Stoliarov, "Characterization of pyrolysis and combustion of rigid poly(vinyl chloride) using two-dimensional modeling," *International Journal of Heat and Mass Transfer*, vol. 132, pp. 347–361, Apr. 2019, doi: 10.1016/j.ijheatmasstransfer.2018.12.011.
- [9] B. Batiot, T. Rogaume, A. Collin, F. Richard, and J. Luche, "Sensitivity and uncertainty analysis of Arrhenius parameters in order to describe the kinetic of solid thermal degradation during fire phenomena," *Fire Safety Journal*, vol. 82. Elsevier Ltd, pp. 76–90, May 01, 2016. doi: 10.1016/j.firesaf.2016.03.007.
- [10] T. Fateh, F. Richard, and T. Rogaume, "Modeling of the pyrolysis of plywood exposed to heat fluxes under cone calorimeter," in *Fire Safety Science*, 2014, vol. 11, pp. 208–221. doi: 10.3801/IAFSS.FSS.11-208.
- [11] C. di Blasi, "Modeling chemical and physical processes of wood and biomass pyrolysis," *Progress in Energy and Combustion Science*, vol. 34, no. 1. pp. 47–90, Feb. 2008. doi: 10.1016/j.peccs.2006.12.001.
- [12] P. Boulet *et al.*, "Characterization of the radiative exchanges when using a cone calorimeter for the study of the plywood pyrolysis," *Fire Safety Journal*, vol. 51, pp. 53–60, Jul. 2012, doi: 10.1016/j.firesaf.2012.03.003.
- [13] N. Gascoin, A. Navarro-Rodriguez, P. Gillard, and A. Mangeot, "Kinetic modelling of high density polyethylene pyrolysis: Part 1. Comparison of existing models," *Polymer Degradation and Stability*, vol. 97, no. 8, pp. 1466–1474, Aug. 2012, doi: 10.1016/j.polymdegradstab.2012.05.008.
- [14] H. Homma, H. Homma, and M. Idris, "Numerical analysis on wood pyrolysis in pre-vacuum chamber," *Journal of Sustainable Bioenergy Systems*, vol. 04, no. 03, pp. 149–160, 2014, doi: 10.4236/jsbs.2014.43014.
- [15] N. A. Liu, W. Fan, R. Dobashi, and L. Huang, "Kinetic modeling of thermal decomposition of natural cellulosic materials in air atmosphere," *Journal of Analytical and Applied Pyrolysis*, vol. 63, no. 2, pp. 323–325, 2002. www.elsevier.com/locate/jaap
- [16] H. E. Kissinger, "Reaction kinetics in differential thermal analysis," *Analytical Chemistry*, vol. 29, no. 11, pp. 1702–1706, Nov. 1957, doi: 10.1021/ac60131a045.

- [17] H. E. Kissinger, "Variation of peak temperature with heating rate in differential thermal analysis," *Journal of Research of the National Bureau of Standards*, vol. 57, no. 4, Oct. 1956.
- [18] D. Cancellieri, E. Leoni, and J. L. Rossi, "Kinetics of the thermal degradation of Erica arborea by DSC: Hybrid kinetic method," *Thermochimica Acta*, vol. 438, no. 1–2, pp. 41–50, Nov. 2005, doi: 10.1016/j.tca.2005.07.013.
- [19] Z. A. Piskulich, O. O. Mesele, and W. H. Thompson, "Activation energies and beyond," *Journal of Physical Chemistry A*, vol. 123, no. 33, pp. 7185–7194, Aug. 2019, doi: 10.1021/acs.jpca.9b03967.
- [20] V. Aquilanti, N. D. Coutinho, and V. H. Carvalho-Silva, "Kinetics of low-temperature transitions and a reaction rate theory from non-equilibrium distributions," *Philosophical Transactions of the Royal Society A: Mathematical, Physical and Engineering Sciences*, vol. 375, no. 2092. Royal Society Publishing, Apr. 28, 2017. doi: 10.1098/rsta.2016.0201.
- [21] E. Amini, M. S. Safdari, J. T. DeYoung, D. R. Weise, and T. H. Fletcher, "Characterization of pyrolysis products from slow pyrolysis of live and dead vegetation native to the southern United States," *Fuel*, vol. 235, pp. 1475–1491, Jan. 2019, doi: 10.1016/j.fuel.2018.08.112.
- [22] P. Fu, W. Yi, X. Bai, Z. Li, S. Hu, and J. Xiang, "Effect of temperature on gas composition and char structural features of pyrolyzed agricultural residues," *Bioresource Technology*, vol. 102, no. 17, pp. 8211–8219, Sep. 2011, doi: 10.1016/j.biortech.2011.05.083.
- [23] M. I. Jahirul, M. G. Rasul, A. A. Chowdhury, and N. Ashwath, "Biofuels production through biomass pyrolysis- A technological review," *Energies*, vol. 5, no. 12. MDPI AG, pp. 4952–5001, 2012. doi: 10.3390/en5124952.
- [24] G. Ningbo, L. Baoling, L. Aimin, and L. Juanjuan, "Continuous pyrolysis of pine sawdust at different pyrolysis temperatures and solid residence times," *Journal of Analytical and Applied Pyrolysis*, vol. 114, pp. 155–162, Jul. 2015, doi: 10.1016/j.jaap.2015.05.011.
- [25] T. Ma, "A thermal theory for estimating the flammability limits of a mixture," *Fire Safety Journal*, vol. 46, no. 8, pp. 558–567, Nov. 2011, doi: 10.1016/j.firesaf.2011.09.002.
- [26] 2017, ASTM E1354: Standard test method for heat and visible smoke release rates for materials and products using an oxygen consumption calorimeter.
- [27] 2003, ASTM E-2058: Standard test methods for measurement of synthetic polymer material flammability using a fire propagation apparatus (FPA).
- [28] G. H. Kwon, S. W. Baek, and Y. M. Sohn, "Ignition of solid fuel by thermal radiation in a confined rectangular enclosure: Experiment and numerical analysis," *Combustion Science and Technology*, vol. 165, no. 1, pp. 85–110, 2001, doi: 10.1080/00102200108935827.
- [29] Y. Nakamura and T. Kashiwagi, "Effects of sample orientation on nonpiloted ignition of thin poly (methyl methacrylate) sheet by a laser: 1. Theoretical prediction," *Combustion and Flame*, vol. 141, no. 1–2, pp. 149–169, Apr. 2005, doi: 10.1016/j.combustflame.2004.12.014.
- [30] N. Bal, "Uncertainty and complexity in pyrolysis modelling," postgraduate dissertation, the University of Edinburgh, Aug. 2012. <https://www.researchgate.net/publication/292611832>
- [31] D. Vamvuka, S. I. Sfakiotakis, D. Vamvuka, N. el Chatib, and S. Sfakiotakis, "Measurements of ignition point and combustion characteristics of biomass fuels and their blends with lignite," at the 7th National Technical Meeting of the Combustion Insititute, Atlanta, Georgia, USA, Mar. 2011. <https://www.researchgate.net/publication/232168026>
- [32] R. E. Lyon and J. G. Quintiere, "Criteria for piloted ignition of combustible solids," *Combustion and Flame*, vol. 151, no. 4, pp. 551–559, Dec. 2007, doi: 10.1016/j.combustflame.2007.07.020.
- [33] F. Z. Sabi *et al.*, "Ignition/non-ignition phase transition: A new critical heat flux estimation method," *Fire Safety Journal*, vol. 119, Jan. 2021, doi: 10.1016/j.firesaf.2020.103257.
- [34] M. J. Hurley *et al.*, *SFPE handbook of fire protection engineering, fifth edition*. Springer New York, 2016. doi: 10.1007/978-1-4939-2565-0.
- [35] X. G. Li, B. G. Ma, L. Xu, Z. W. Hu, and X. G. Wang, "Thermogravimetric analysis of the co-combustion of the blends with high ash coal and waste tyres," *Thermochimica Acta*, vol. 441, no. 1, pp. 79–83, Feb. 2006, doi: 10.1016/j.tca.2005.11.044.

- [36] J. L. Cordova, D. C. Walther, J. L. Torero, and A. C. Fernandez-Pello, "Oxidizer flow effects on the flammability of solid combustibles," *Combustion Science and Technology*, vol. 164, no. 1–6, pp. 253–278, 2001, doi: 10.1080/00102200108952172.
- [37] J. Quintiere, "A Simplified Theory for Generalizing Results from a Radiant Panel Rate of Flame Spread Apparatus." *Fire and Materials*, vol. 5, pp. 52-60. Jun. 1981. <https://doi.org/10.1002/fam.810050204>.
- [38] N. P. Setchkin, "A method and apparatus for determining the ignition characteristics of plastics." *Journal of Research of the National Bureau of Standards*, vol. 43, 1949. https://nvlpubs.nist.gov/nistpubs/jres/43/jresv43n6p591_A1b.pdf
- [39] V. Babrauskas, "Ignition of wood: A review of the state of the art," *Journal of Fire Protection Engineering*, vol. 12, no. 3, pp. 163–189, 2002, doi: 10.1177/10423910260620482.
- [40] S. McAllister, M. Finney, J. Cohen, 2011. Critical mass flux for flaming ignition of wood as a function of external radiant heat flux and moisture content. In: 7th US National Technical Meeting of the Combustion Institute; Georgia Institute of Technology, Atlanta, GA; 20-23 March 2011. 1: 1698-1704.
- [41] M. A. Delichatsios, "Piloted ignition times, critical heat fluxes and mass loss rates at reduced oxygen atmospheres," *Fire Safety Journal*, vol. 40, no. 3, pp. 197–212, Apr. 2005, doi: 10.1016/j.firesaf.2004.11.005.
- [42] D. Rich, C. Lautenberger, J. L. Torero, J. G. Quintiere, and C. Fernandez-Pello, "Mass flux of combustible solids at piloted ignition," *Proceedings of the Combustion Institute*, vol. 31 II, pp. 2653–2660, 2007, doi: 10.1016/j.proci.2006.08.055.

Chapter 3. EXPERIMENTAL METHODOLOGY

3.1 Experimental set-up

The cone calorimeter is a bench-scale fire testing apparatus, which has been developed by NIST, to measure the flammability of materials. A cone calorimeter consists of the following components: a conical radiant electric heater, capable of horizontal or vertical orientation; specimen holders, different for the two orientations; an exhaust gas system with oxygen monitoring and flow measuring instrumentation; an electric ignition spark plug; a data collection and analysis system; and a load cell for measuring specimen mass loss. The apparatus schematic is shown in Figure 3.1. When testing, specimens are burned in ambient conditions with a predetermined heat flux, which can be set up to 100 kW/m^2 [1]. The test permits the ignition either with or without the spark igniter. The measurements include the oxygen concentration, mass-loss rate of the specimen, time to ignition and smoke obscuration.

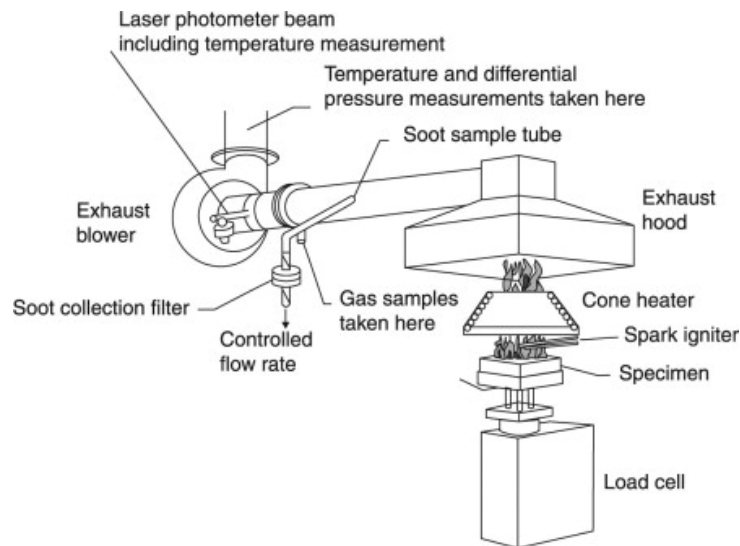


Figure 3.1 Schematic of the cone calorimeter for its original design [1]

The calorimeter used in this work was modified to study the pyrolysis and ignition mechanisms of pine needles, as shown in Figure 3.2. The modifications consisted in adding a custom-designed cylindrical testing chamber that allows an inflow of air or nitrogen through the sample with desired flow rates, adding a sampling probe on top of the testing chamber connected to a Fourier-transform infrared

(FTIR) spectrometer to collect and characterize the pyrolysis gases for the pyrolysis tests, and a radiation shield to avoid the preheating of the fuel.

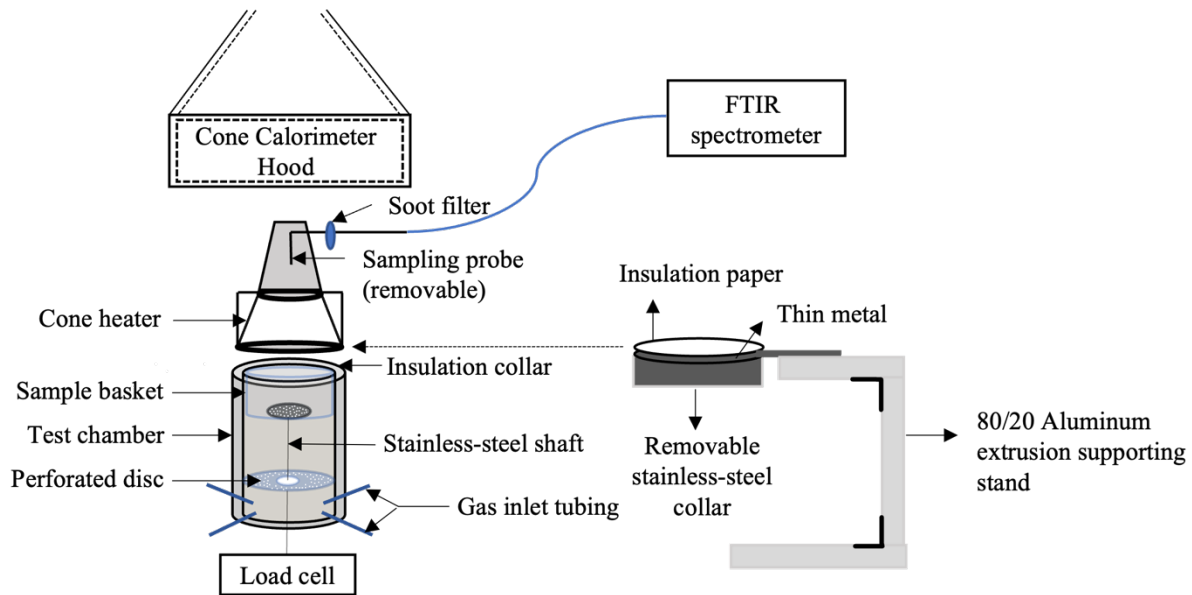


Figure 3.2 Experimental apparatus: modified cone calorimeter allowing for gas inflow through the sample and pyrolysis gas measurement.

The 304 mm tall testing chamber consists of one layer of a 6-mm-thick ceramic bucket, one layer of 25.4-mm-thick ceramic insulation wool, and one layer of 3.05-mm-thick stainless-steel shell. The stainless-steel hard shell with inner and outer diameters of 146.30 mm and 152.4 mm, respectively, is placed outside the insulation wool to attach the air inlet tubes and to protect the middle layer of insulation wool from wear. The high-temperature resistant ceramic bucket with inner and outer diameters of 140 mm and 146 mm, respectively is the innermost layer of the testing chamber. At a height of 50 mm from the bottom of the testing chamber, four holes are drilled evenly along the circumference. Four 6.35 mm gas tubes are inserted through the holes to introduce nitrogen or air with desired flow rates. A circular stainless steel perforated disk with a diameter of 146 mm and a porosity of 48% was fixed inside the testing chamber and placed 40 mm above the gas tubing to mix the introduced gases. A sample basket holder, made of a stainless-steel shaft and a platform with 48% porosity stands in the center of the testing chamber, connecting the load cell to the sample basket.

The radiation shields consist of a 203 mm × 203 mm square steel sheet with a thickness of 1.91 mm covered by a layer of 1.91 mm-thick ceramic insulation paper. The shield is supported by a stand, which allows the shield to be positioned beneath the bottom of the conical heater to prevent the preheating of the sample and is removed when the test is started. For the pyrolysis tests, a 20 mm-high stainless-steel collar with a 145 mm-diameter is attached to the steel sheet to avoid the oxidization of the pyrolysis gases during their transportation to the sampling probe.

A 6.10 mm diameter stainless steel sampling probe, fixed inside a steel funnel that sits just above the conical heater and completely covers the opening of the heater, is used to collect the pyrolysis gas. A 50 mm-diameter WHATMAN HEPA-vent filter is added to the outlet of the sampling probe to prevent soot clogging. The pyrolysis gas is sampled right above the conical heater using the sampling probe and pumped into the gas cell of the FTIR spectrometer (Nicolet iS10) with a sampling rate of 2 l/min.

The cone heater consists of an electrical heater rod that is wound into a truncated cone and is capable of producing irradiance to the sample surface up to 100 kW/m². The irradiance of the cone heater can be kept at a preset level through a temperature controller whose range is 0 to 1000 °C and three type-K stainless steel thermocouples [1]. The thermocouples are connected in parallel, looping around the heating element, with the beads touching the heating element. This arrangement was found to give quick and stable control for the cone temperature when the specimen flame impinges on the cone [2].

The exhaust gas system of the cone calorimeter consists of an exhaust fan, a hood, an exhaust duct for the fan, a gas sampler, a gas analyzer, a thermocouple, and an orifice plate. It monitors O₂, CO, and CO₂ concentrations, as well as measures the temperature and flow rate of the exhaust flow.

The digital collection system records the outputs from the oxygen analyzer, the orifice plate, the thermocouples, and the load cell with a 1 Hz frequency. The heat release rate is determined based on the readings from the oxygen analyzer and flow rate from the exhaust system [2].

3.2 Sample preparation

The vegetation fuel used in this thesis was dead needles from *Pinus palustris* that are mainly distributed in the southern US and are of high flammability [3]. An oven-drying process was followed to determine the moisture content of the pine needles for 24 h at 60 °C [4, 5]. The conditioned needles were stored in sealed containers before testing. The fuel properties, determined before the tests, include moisture content (FMC) on a dry basis, density (ρ_{needle}), and bulk density (ρ_{bulk}). These properties were computed according to Eq (3.1) - Eq (3.3) and listed in Table 3.1. The uncertainty of these fuel properties was determined by one standard deviation of the fuel samples prepared for each test.

$$FMC (\%) = \frac{m_{bd} - m_{ad}}{m_{ad}} \times 100 \quad \text{Eq (3.1)}$$

$$\rho_{needle} = \frac{m_{ad}}{V_{ad}} \quad \text{Eq (3.2)}$$

$$\rho_{bulk} = \frac{m_{ad}}{V_{basket}} \quad \text{Eq (3.3)}$$

Where m_{bd} and m_{ad} are the sample masses before and after oven-drying; V_{ad} and V_{basket} are respectively the net sample volume after oven-drying and the sample basket volume. By immersing a known mass oven-dried pine needles in a known volume of water, the V_{ad} is determined based on the volume displaced by the fully immersed needles.

Table 3.1 Fuel properties

Sample	FMC (%)	ρ_{needle} (kg/m ³)	ρ_{bulk} (kg/m ³)
<i>Pinus palustris</i> pine needles	4.6 (± 2.8)	526.9 (± 16.8)	38.5 (± 0.2)

For the experiments, 20 g of conditioned pine needles were placed in a cylindrical sample holder 12.6 cm in diameter and 3 cm in depth. Two different types of sample holders were used. For the experiments with no inflow of oxidizer being fed through the bottom of the combustion chamber (buoyancy-induced flow), a sample holder with 0% porosity was used. On the other hand, for experiments with a forced inflow being supplied, a sample holder with 63% porosity was used. A porosity of 63%

rather than 48% was chosen to allow for a more uniform flow within the sample holder [6]. Figure 3.3 presents images of the test samples used for both types of experiments.

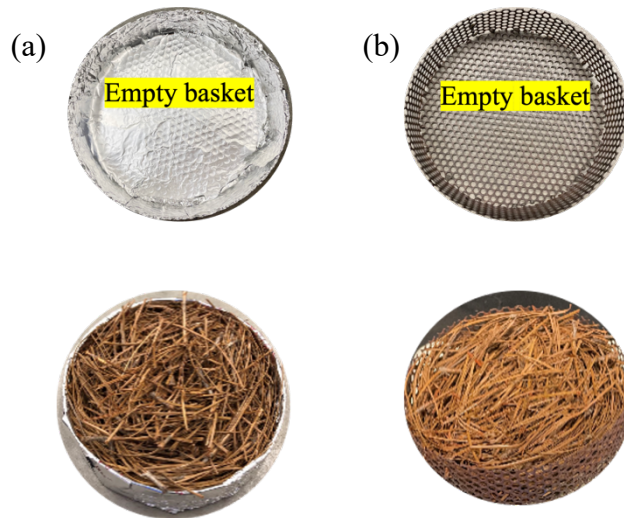


Figure 3.3 Fuel samples for the tests with (a) buoyancy-induced flow using the basket of 0% opening and (b) forced flow using the basket of 63% opening

3.3 Experimental methods

3.3.1 Apparatus Calibration and Validation

Two apparatuses used in this work are the modified cone calorimeter (CC) and an FTIR spectrometer. Both experimental apparatuses are required to be calibrated or validated before tests to ensure that the testing results can be confidently viewed as accurate and reliable.

For the modified cone calorimeter, calibrations of the heat flux, oxygen analyzer, heat release rate, load cell, and smoke obscuration measuring system are performed in accordance with section 10 of ASTM E 1354-17.

The heat flux calibration is conducted by placing a reference Schmidt-Boelter heat flux sensor 25 mm away from the base plate of the conical heater at the same height where the upper surface of the fuel sample bed will be placed during testing. The irradiance level of the cone heater is controlled by the cone calorimeter temperature controller and the three K-thermocouples that are connected to the temperature controller. The measured voltage of the pre-calibrated heat flux sensor has a linear response to the

irradiance level of the conical heater. The actual radiant heat flux received by the heat flux sensor is obtained by multiplying the regression factor of the linear response (provided by the supplier) with the voltage output. The resultant heat flux calibration curve for the modified cone calorimeter is shown in Fig 3.4. The temperature in the plot is the average value of the readings from the three thermocouples of the conical heater.

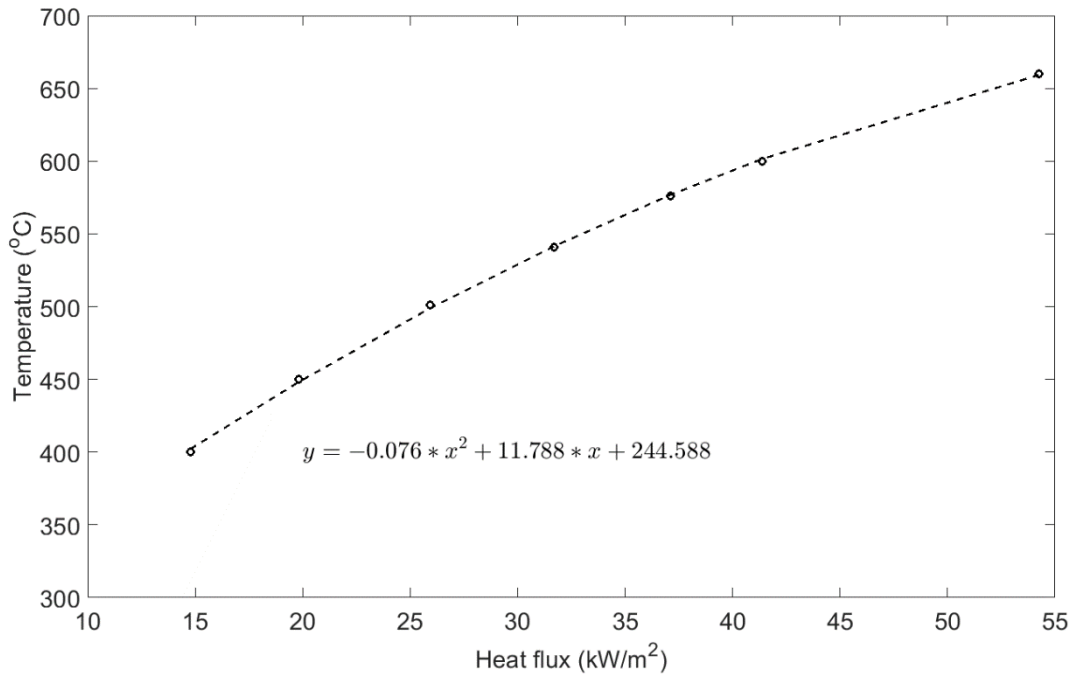


Figure 3.4 Cone heater heat flux calibration

The calibration for the oxygen analyzer consists of a daily verification for the accuracy of O₂ volume concentration measurements and the checking for the analyzer delay time, t_d . The daily verification for the measurement accuracy is made by adjusting the analyzer responses using O₂ with volume fractions of 0% and 20.95%, respectively. With a 5 kW methane fire supplied by the burner, the delay time of the analyzer (t_d) is determined, by the time difference between the time when the temperature reading changes more than 8°C and the time when O₂ volume percentage varies greater than 0.75% [1], as 31s. During the whole period of the experimental campaign of this work, this delay time did

not vary. Therefore, the O₂ measurement during testing ($X_{O_2_{meas}}$) is corrected based on the delay time (t_d). The O₂ reading after correction at time t ($X_{O_2_{cor}}(t)$) is shown in Eq (3.4).

$$X_{O_2_{cor}}(t) = X_{O_2_{meas}}(t - t_d) \quad \text{Eq (3.4)}$$

The calibration of the heat release rate is required at the start of testing each day to evaluate the performance of the flow meter. The procedure is to obtain a calibration constant, C by introducing pure methane with a flow rate corresponding to 5 kW to the calibration burner. The constant obtained from the calibration should not be more than 5% different from the previously calibrated one, and will be used to calculate the heat release rate of a testing material, shown as Eq (3.5) [1].

$$HRR(t) = \left(\frac{\Delta h_c}{r_o}\right) (1.10) C \sqrt{\frac{\Delta P}{T_e} \frac{(X_{O_2}^0 - X_{O_2}(t))}{1.105 - 1.5X_{O_2}(t)}} \quad \text{Eq (3.5)}$$

Where $\left(\frac{\Delta h_c}{r_o}\right)$ is 13.1×10^3 kJ/g, representing the heat released per 1 kg of oxygen consumed by a hydrocarbon fuel; C is the resultant constant from the heat release rate calibration; ΔP and T_e are the pressure differential and absolute gas temperature measured from the orifice meter; $X_{O_2}^0$ and $X_{O_2}(t)$ are readings from the oxygen analyzer at the initial and time t .

The load cell has a 0.01g accuracy and is calibrated with six different standard weights: 0 g, 50 g, 100 g, 150 g, 200 g, and 230 g. The laser calibration is performed using four different neutral filters with 0%, 30%, 80%, and 100% transmission.

The validation of the FTIR spectrometer includes [7]:

- system configuration identification,
- limit of detection (LOD) check,
- wavenumber accuracy check,
- system response time evaluation.

The system configuration contains a set of parameters that guarantee the result's reproducibility for a particular FTIR system. This set includes the minimum instrumental linewidth (MIL) that is a measure of instrument resolution, the absorption pathlength (The spectrometer with a 2-meter absorption

pathlength is used in this work.), the apodization function modifying the generated interferogram, the gas temperature, the gas pressure, the zero-filling factor added to the end of a measured interferogram, the measured wavenumbers of two specific water absorption bands, the reference spectra sources, the integration time over which the selected number of scans is executed (16 scans for each spectrum in this work), and the detector type. The FTIR system configuration in this work is listed in Table 3.2.

Table 3.2 FTIR spectrometer system configuration

Spectrometer	Nicolet iS10 [®]
MIL	1.69 cm ⁻¹
Resolution	2 cm ⁻¹
Absorption pathlength	2 meters
Apodization function	N-B strong
Gas temperature	28.5 °C
Gas pressure	301.6 ± 5.8 mmHg
Zero filling factor	2
Wavenumbers of water bands	1652 cm ⁻¹ and 3744 cm ⁻¹
Reference library sources	EPA spectral database
Integration time	26.3 seconds (16 scans)
Detector type	MCT
Detector gain	4.0

The LOD check, fundamental to further quantitative analysis of analyte concentrations, requires the values of residual squared area (RSA) for each analyte in corresponding analytical regions from a workspace air spectrum. The RSA reflects the noise level in each analytical region of a spectrum and is calculated by Eq (3.6). Combining the calculated RSA values and characteristics of both reference and sample spectra, the LOD can be determined based on Eq (3.7).

$$RSA = \frac{[w_q - w_p]}{q - p + 1} \sqrt{\sum_{i=p}^{i=q} \frac{(R_i)^2}{q - p}} \quad \text{Eq (3.6)}$$

$$LOD = \frac{(CCP)(RSA)}{LA_R} \quad \text{Eq (3.7)}$$

Where w_p to w_q (unit: cm⁻¹) is the wavenumber range for an analytical region; p to q is the number of data points in the range of w_p to w_q ; R_i is the absorbance value from a residual spectrum in the corresponding analytical region; CCP (unit: ppm-m) is the product of the concentration and pathlength of

the reference spectrum; L (unit: m) is the absorption pathlength of the sample spectrum; and A_R (unit: $\text{abs}\cdot\text{cm}^{-1}$ where “abs” means absorbance) is the absorbance area of a reference spectrum in the corresponding analytical region.

To obtain the discrete absorbance value R_i in Eq (3.6) for an analytical region, a residual spectrum is required, which can be formed by subtracting the scaled reference spectra from a workspace air spectrum. For each analytical region, the determination of the scaling factor should meet the requirement of minimizing the absorbance in the resulting difference spectrum. Considering the components present in the workspace air, the selection of the references in this work is the spectra of water vapor and carbon dioxide.

The analytes of interest in this work are the pine needle’s pyrolysis gas constituents that are found to consist of CH_4 , CO , CO_2 , and H_2O based on their characteristic bands (See chapter 4). Each of these constituents at least shows one unique characteristic band in an FTIR spectrum. Each characteristic band corresponds to an analytical region. However, only the ones having the most obvious absorption peaks are selected and used for quantification analysis in this work. According to the reference spectra of these four constituents from the EPA database [7] (see Figure 3.5), the selected analytical regions, RSAs, and LODs for these pyrolysis gas constituents are selected, computed, and listed in Table 3.3.

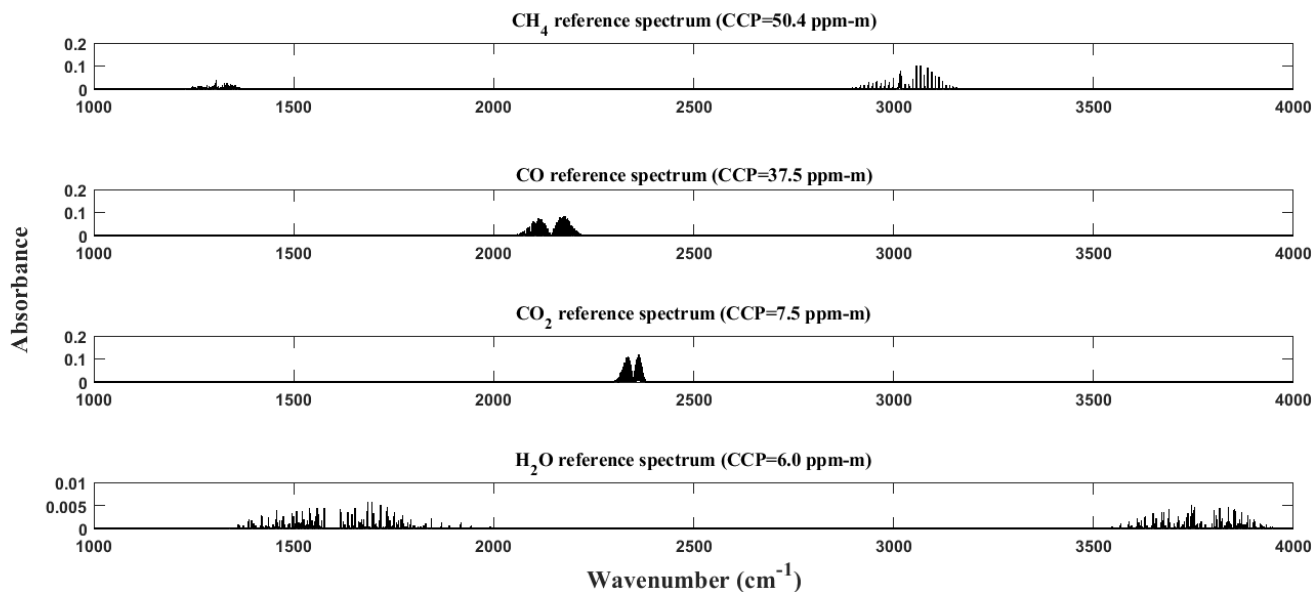


Figure 3.5 Reference spectra for CH_4 , CO , CO_2 , and H_2O from the EPA spectra database [7]

Table 3.3 RSA and LOD analysis for target pyrolysis constituents

Analytical region (cm^{-1})	Species	Reference Spectra			System Configuration		
		File name	CCP (ppm-m)	Absorbance area ($abs - cm^{-1}$)	RSA ($abs - cm^{-1}$)	L (m)	Estimated LOD (ppm)
2880~3180	CH_4	ch4300.spc	50.4	0.18	1.97E-07	2.0	2.69E-05
2010~2250	CO	co300.spc	37.5	0.39	2.38E-07	2.0	1.14E-05
2290~2390	CO_2	co2300.spc	7.5	0.77	2.87E-09	2.0	1.39E-08
1390~2020	H_2O	h2o300.spc	6	0.07	1.34E-05	2.0	6.13E-04
3500~3998				0.05	4.39E-06	2.0	2.72E-04

A Wavenumber accuracy (RWA) check helps to determine if the wavenumber scale of an FTIR system is appropriate for comparison with reference spectra when requiring quantitative analysis. The detailed procedures of RWA check are described as the following five steps:

- (Step 1) Prepare a workspace air spectrum and a reference water vapor spectrum.
- (Step 2) From the workspace air spectrum, determine the wavenumber values of two water vapor absorption features as w_{S1} and w_{S2} in the corresponding analytical regions;

The wavenumbers of w_{S1} and w_{S2} are required to be at least 500 cm^{-1} away from each other.

- (Step 3) From the reference water vapor spectrum, using the same absorption features that have been applied to determine w_{S1} and w_{S2} from the workspace air spectrum in Step 2, determine the wavenumber values of two water vapor absorptive features as w_{R1} and w_{R2} .
- (Step 4) Calculate RWA values according to Eq (3.8). The calculated result is listed in Table 3.4.

$$RWA = ABS(w_{Ri} - w_{Si}) \quad \text{Eq (3.8)}$$

where *ABS* means the absolute function.

Table 3.4 RWA check for the FTIR system configuration

w_{Ri}	w_{Si}	RWA	RWA/MIL
1652.396	1652.766	0.370	-
3744.664	3744.276	0.388	23.0%

- (Step 5) Based on the identified FTIR system configuration, compare the maximum ratios of RWA/MIL, and check if the value is greater than 2%. If $(RWA/MIL)_{\max}$ is greater than 2%, the sample spectrum needs to be shifted accordingly to match the wavenumber of the reference spectrum [5]. Since the computed RWA/MIL is 23.0%, the sample spectrum should be moved forward 0.38 cm^{-1} when comparing to a reference spectrum.

The FTIR system response time is the minimum time required for the system output to accurately reflect a sudden change in the sample gas composition. To identify the system response time, pure N_2 is first used to purge the sampling line and corresponding sample spectra are recorded at a 30 s interval. Then pure CH_4 with a flow rate of 2 l/min is suddenly introduced into the sampling interface together with 50 l/min of N_2 . Finally, the system response time is the duration required to generate a sample spectrum from

which the measured CH₄ concentration reaches 95% of its final concentration. In this work, the response time was determined as 26.3 s.

3.3.2 Test design and procedures

Two series of experiments were conducted using the modified cone calorimeter to understand the mechanisms driving the ignition of dead *Pinus palustris* needles. In the first set of experiments, Fourier-transform infrared spectroscopy (FTIR) was used to characterize the composition of the pyrolysis gases generated from the thermal degradation of pine needles when the fuel bed was exposed to incident heat fluxes of 20 and 30 kW/m², and a nitrogen inflow of 50 l/min. The main constituents of the pyrolysis gas were identified by the characteristic bands shown in FTIR scans and were quantified by applying Beer-Lambert's law [7, 8]. The test procedure for the pyrolysis test is shown in Table 3.5.

Table 3.5 Pyrolysis test procedure

Test time	Event
Pre-test preparation	Check the CC load cell reading; make sure the pump and the exhaust fan are on.
	Open the valve for compressed air, set the flow rate as desired (0, 50, and 100 l/min).
	Place the sample basket on the sample holder and adjust the height of the sample so that its surface is at the same level as the top edge of the testing chamber.
	Cover the testing chamber with the modified radiation shield to prevent the sample preheating.
	Turn on and set the temperature controller to the desired value, then wait until it stabilizes (5 min at least).
	Prepare the video recording using a high-speed camera with a 240 fps frame rate.
0 s	Use the entire FTIR system to record an absorbance spectrum of N ₂ to verify the absence of contaminants in the sampling system and infrared absorption cell.
	Open the valve between the sampling line and the FTIR gas cell and wait until the temperature and pressure of the gas cell stabilize.
	Start CC data collection for ambient and collect a sample spectrum.
	Remove the radiation shield and slide the spark igniter so that the spark is activated directly above the center of the fuel bed.
	Start the continuous pyrolysis gas FTIR spectrum collection with a 2 cm ⁻¹ resolution (the collection time for each spectrum is 26.3 s).
	Stop the FTIR spectrum collection.
480 s	Stop CC data collection. Turn off the cone heater.

In the second set of experiments, the ignition of pine needles was studied for varied incident heat fluxes (20 to 35 kW/m²) and air flow rates (buoyancy-induced, 50 and 100 l/min forced flow). A high-resolution high-speed camera acquiring videos at 240 fps was used to accurately determine the time-to-ignition (t_{ig}), and the exact location of ignition. In these tests, the time-to-ignition (t_{ig}), the critical mass-

loss rate at ignition (\dot{m}''_{cr}), and the heat release rate per unit area at ignition ($HRRPUA_{ig}$) were evaluated.

The corresponding test procedure is shown in Table 3.6.

Table 3.6 Ignition test procedure

Test time	Event
Pre-test preparation	Check the CC load cell reading. Make sure the pump and the exhaust fan are on.
	Open the valve for compressed air, set the flow rate as desired (0, 50, and 100 l/min).
	Place the sample basket on the sample holder and adjust the height of the sample so that its surface is at the same level as the top edge of the testing chamber.
	Cover the testing chamber with the modified radiation shield to prevent the sample preheating.
	Turn on and set the temperature controller to the desired value, then wait until it stabilizes (5 min at least).
	Prepare the video recording using a high-speed camera with 240 fps frame rate.
0 s	Start CC data collection at the ambient temperature and the video recording.
90 s	Remove the radiation shield and slide the spark igniter so that the spark is activated directly above the center of the fuel bed.
600 s	Stop CC data collection, video recording and turn off the cone heater.

For all the experimental conditions tested, three repetitions were performed. Table 3.7 presents a summary of the experimental conditions.

Table 3.7 Experimental matrix.

Species	Sample mass (g)	Type of test	Heat flux (kW/m ²)	Flow rate (l/min)	Atmosphere (vol. %)
Pinus palustris	20.52 ± 2.17	Pyrolysis	20, 30	50	100% N ₂
		Ignition	20, 25, 30, 35	0, 50, 100	Lab air

3.4 References

- [1] 2017, ASTM E1354: Standard test method for heat and visible smoke release rates for materials and products using an oxygen consumption calorimeter.
- [2] V. Babrauskas, “Development of the cone calorimeter -- a bench-scale heat release rate apparatus based on oxygen consumption,” Gaithersburg, MD, 1982. doi: 10.6028/NBS.IR.82-2611.
- [3] R. K. Emery and J. L. Hart, “Flammability characteristics of surface fuels in a longleaf pine (*Pinus palustris* mill.) woodland,” *Fire*, vol. 3, no. 3, pp. 1–18, Sep. 2020, doi: 10.3390/fire3030039.
- [4] P. Bartoli, A. Simeoni, H. Biteau, J. L. Torero, and P. A. Santoni, “Determination of the main parameters influencing forest fuel combustion dynamics,” *Fire Safety Journal*, vol. 46, no. 1–2, pp. 27–33, Jan. 2011, doi: 10.1016/j.firesaf.2010.05.002.
- [5] Plummer, G., M., Reagen, W., K., & Logan, P., W. (2003). Organic and inorganic gases by extractive FTIR spectrometry. *NIOSH Manual of Analytical Methods, Fourth Edition*. <https://www.cdc.gov/niosh/docs/2003-154/pdfs/3800.pdf>
- [6] R. Liu, D. S. K. Ting, and G. W. Rankin, “On the generation of turbulence with a perforated plate,” *Exp Therm Fluid Sci*, vol. 28, no. 4, pp. 307–316, 2004, doi: 10.1016/S0894-1777(03)00106-7.
- [7] US EPA. (2003). Test method 320: Measurement of vapor phase organic and inorganic emissions by extractive Fourier Transform Infrared (FTIR) Spectrometry. <https://www.ecfr.gov/>
- [8] US EPA. (2016, February 23). Emission measurement center spectral database. EPA. <https://www3.epa.gov/ttn/emc/ftir/welcome.html>

Chapter 4 RESULTS AND DISCUSSION

In this chapter, the results of the experiments conducted are analyzed. For the pyrolysis tests, the pyrolysis gas of dead pine needles is characterized in terms of constituent composition and concentration under different external heat fluxes (20 and 30 kW/m²) and a constant flow of 50 l/min nitrogen. For the ignition tests, the variation of the ignition position, time to ignition (t_{ig}), mass loss rate per unit area at ignition ($MLRPUA_{ig}$), and heat release rate per unit area at ignition ($HRRPUA_{ig}$) under different external heat fluxes (20 to 30 kW/m²) and flow conditions (buoyancy-induced, 50 and 100 l/min forced flow) are discussed.

4.1 Pyrolysis tests

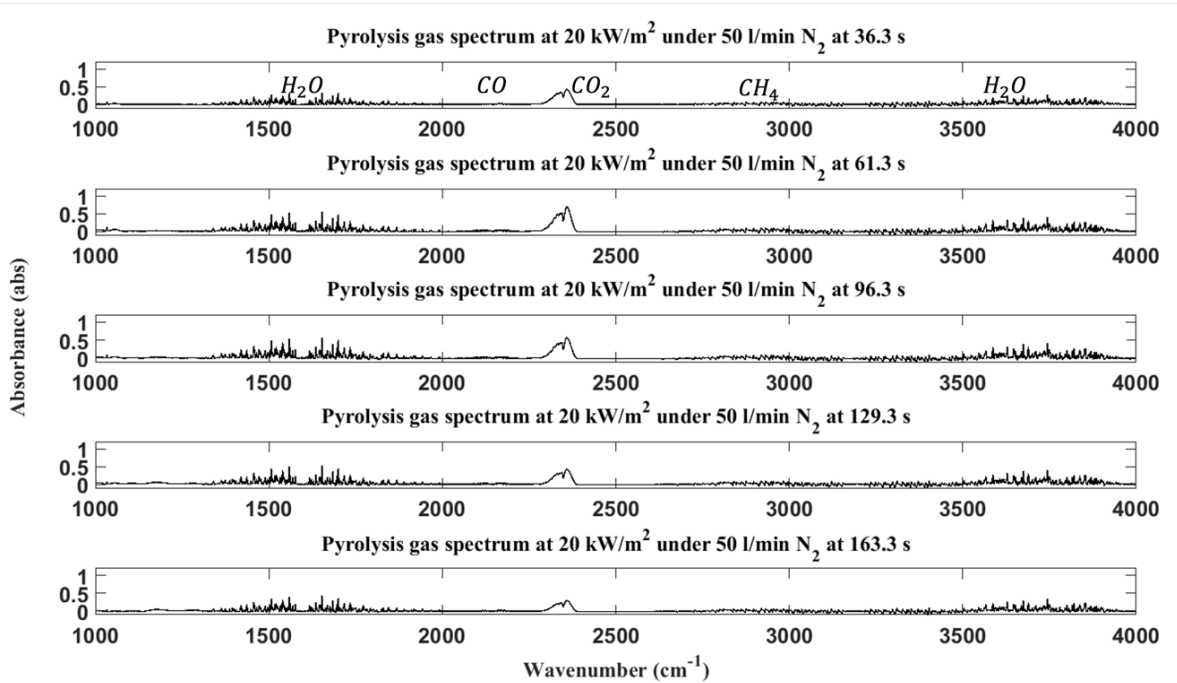
4.1.1 Pyrolysis gas component identification

Figure 4.1 presents the FTIR spectra of the pyrolysis gas samples collected during the experiments conducted at incident heat flux of 20 and 30 kW/m², respectively. The strong characteristic bands at 2880-3180 cm⁻¹, 2010-2250 cm⁻¹, and 2290-2390 cm⁻¹ indicate the formation of CH₄, CO, and CO₂. The characteristic bands at 1390-2020 cm⁻¹ and 3500-3998 cm⁻¹ represent the occurrence of H₂O. The same pyrolysis gas components of plant species are also found in the literature [1-4]. However, the presence of small amounts of heavier hydrocarbons (such as ethane and ethylene that are found in [4] with very low concentrations) cannot be excluded as they share the same absorption characteristics band as CH₄ and are difficult to distinguish. Nevertheless, these heavier hydrocarbons are not considered in the quantification process (Section 4.1.2) because the total hydrocarbon measurement is insensitive to those hydrocarbons that are present in only very small amounts [5].

The spectra of the pyrolysis gases at different heat flux levels have similar absorption bands but different absorbance levels. This observation suggests that varying incident heat fluxes does not change the constitution of the pyrolysis gas but significantly change the percentage of each component in it. From the two spectra sets, most of the pyrolysis gas yields (except for H₂O) significantly increase with external

heat fluxes. The peaks for the characteristic bands of CO, CO₂, and CH₄ are higher at 30 kW/m² than those at 20 kW/m² which, according to Beer's law, reflects a greater release of these components at a higher heat flux. This trend was also reported by [6-8].

(a)



(b)

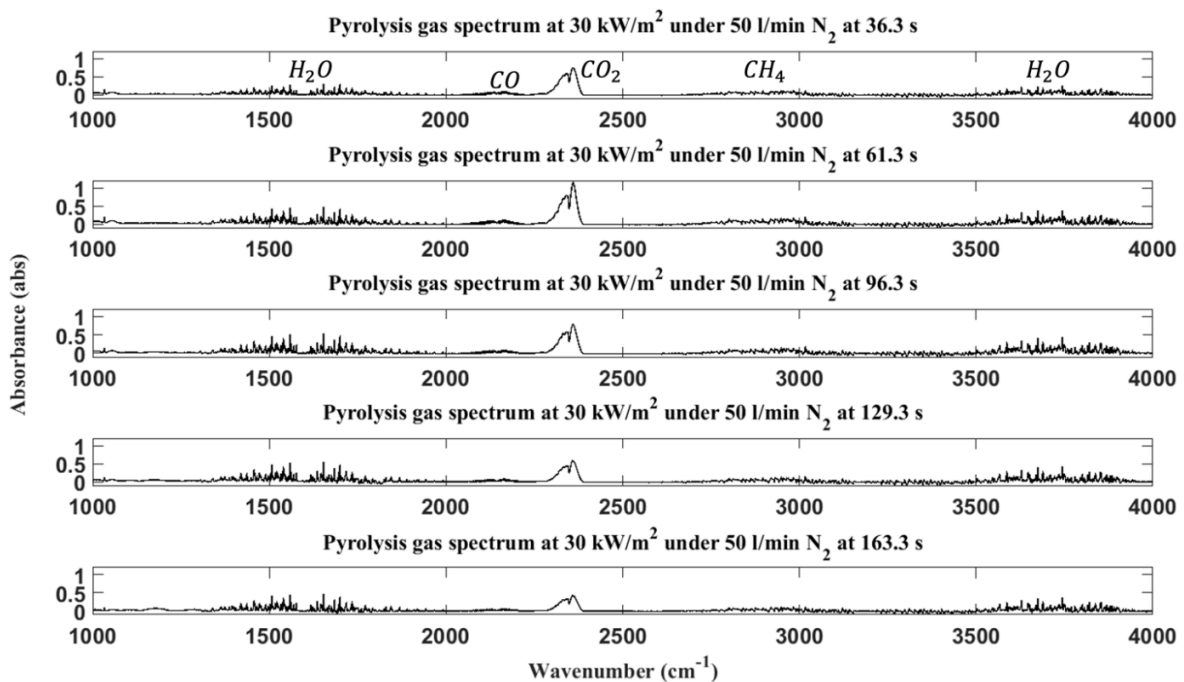


Figure 4.1 Pyrolysis gas FTIR spectra at 50 l/min N₂ and (a) 20 kW/m², 50 l/min N₂ and (b) 30 kW/m².

4.1.2 Quantification of the pyrolysis process

Figure 4.2 shows the evolution of the volume concentration of the different gas species identified in the pyrolysis gas samples collected at both heat flux levels. The evolution of water vapor is omitted in the plot to highlight the variation of the carbon-based compounds, but its share to the pyrolysis gas composition is still taken into account when estimating the concentration of each gas component. All the results are averaged from three repetitions. The uncertainties are determined by $\pm 1\sigma$ of three repetitions. It is essential to highlight that the calculated concentration of each component at each moment is not the instantaneous concentration at that moment, but the average concentration over time of the data collection (26.3 s). Therefore, in the following discussion (specifically Figure 4.2), the concentration of each gas component at ignition refers to the average concentration over a period close to the time of ignition rather than the instantaneous one at ignition.

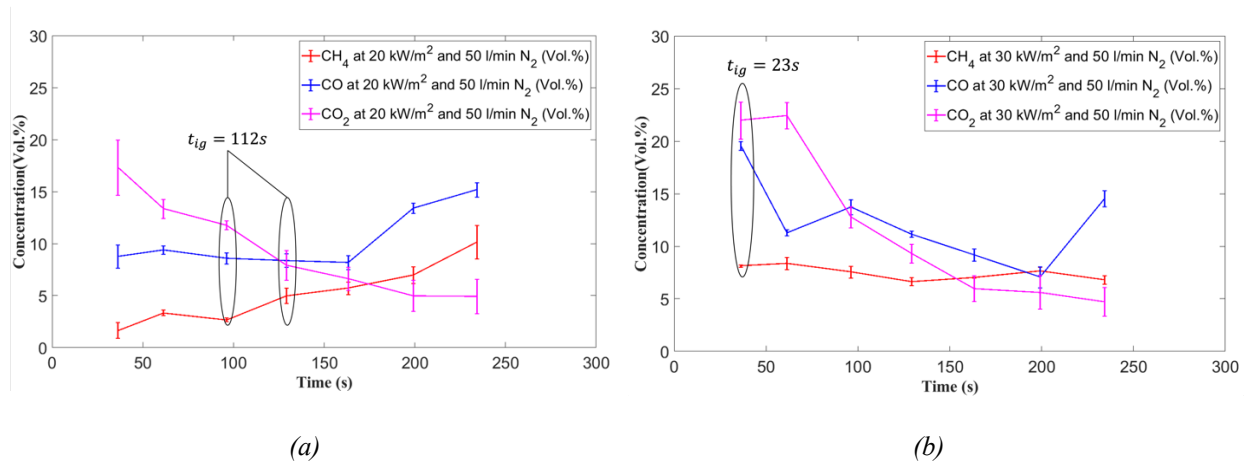


Figure 4.2 Pyrolysis gas volume concentration evolution at (a) 20 kW/m², 50 l/min N₂ and (b) 30 kW/m², 50 l/min N₂. The concentrations of each gas species at t_{ig} were determined by combining the observed time-to-ignition values in the ignition tests (See section 4.2).

In addition to H₂O (which has been omitted from Figure 4.2 to highlight the values of carbon-based gas species), the major pyrolysis gas products are CO and CO₂ at both 20 and 30 kW/m². The average volume concentrations of CH₄, CO, CO₂, and H₂O in the pyrolysis gas obtained under 20 and 30 kW/m² are listed in Table 4.1. The low proportion of CH₄, and the high account of CO and CO₂ in the pyrolysis gas of vegetation were also reported by Amini [2] and Fu [3].

Table 4.1 Average concentration of each gas component in the pyrolysis gas (vol.%)

Heat flux	Ave. X (CH ₄)	Ave. X (CO)	Ave. X (CO ₂)	Ave. X(H ₂ O)
20 kW/m ²	5.1%	10.3%	9.6%	75.1%
30 kW/m ²	7.5%	12.4%	11.8%	64.9%

The results of Ningbo et al. [6] suggest that the changes in concentrations with the heat flux are linked to the secondary cracking of the pyrolysis vapors or the decomposition of the long chains of carbon, hydrogen and oxygen compounds in biomass into smaller fragments at a higher pyrolysis temperature.

Furthermore, combining the results presented above with the time-to-ignition results from the second set of experiments (see Section 4.2), it is possible to evaluate the composition of the pyrolysis gases at ignition. The volume concentrations of CH₄, CO, and CO₂ in the pyrolysis gas at ignition are listed in Table 4.2 for the incident heat flux of 20 and 30 kW/m².

Table 4.2 Concentration of each gas component at ignition (vol.%)

Heat flux	X (CH ₄) at ignition	X (CO) at ignition	X (CO ₂) at ignition	X (H ₂ O) at ignition
20 kW/m ²	3.8%	8.5%	9.9%	77.8%
30 kW/m ²	8.1%	19.6%	22.0%	44.1%

Thus, the effective heat of combustion of these pyrolysis gas mixtures (H_{c_pyr}) can be evaluated as the weighted sum of the heats of combustion of each flammable species, defined by Eqs. (4.1) and (4.2).

$$H_{c_pyr} = Y_{CO} \cdot H_{c_CO} + Y_{CH_4} \cdot H_{c_CH_4} \quad \text{Eq (4.1)}$$

$$Y_i = \frac{X_i M_i}{\sum X_i M_i} \quad \text{Eq (4.2)}$$

where X_i , M_i , Y_i , and H_{c_i} are the mole fraction, molecular weight, mass fraction, and heat of combustion of a given gas species, respectively. The reference values of the heat of combustion of CH₄ and CO are 50.1 and 10.1 kJ/g, respectively [9].

The resulting heat of combustion of the pyrolysis gases was evaluated to be respectively 2.6 kJ/g and 6.4 kJ/g for 20 and 30 kW/m² with the details of uncertainty analysis presented in Appendix A. This

result is in general agreement with the range of heat of combustion values for pyrolysis gas of vegetative fuels (from 4.62 to 5.38 kJ/g) reported by [10]. The variation of the heat of combustion for different heat fluxes indicates that the pyrolysis gas obtained at a higher heat flux is of greater energy.

4.2 Ignition tests

4.2.1 Visual observations at ignition

Figure 4.3 shows the position of the flame at ignition under different experimental conditions. For the experiments conducted with no forced inflow of air through the sample holder and for all incident heat fluxes tested, the ignition of the fuel bed occurred within the vicinity of the spark igniter. For the experiments conducted with a forced inflow of air and for all incident heat fluxes tested, the ignition of the fuel bed occurred at the surface of the fuel bed.

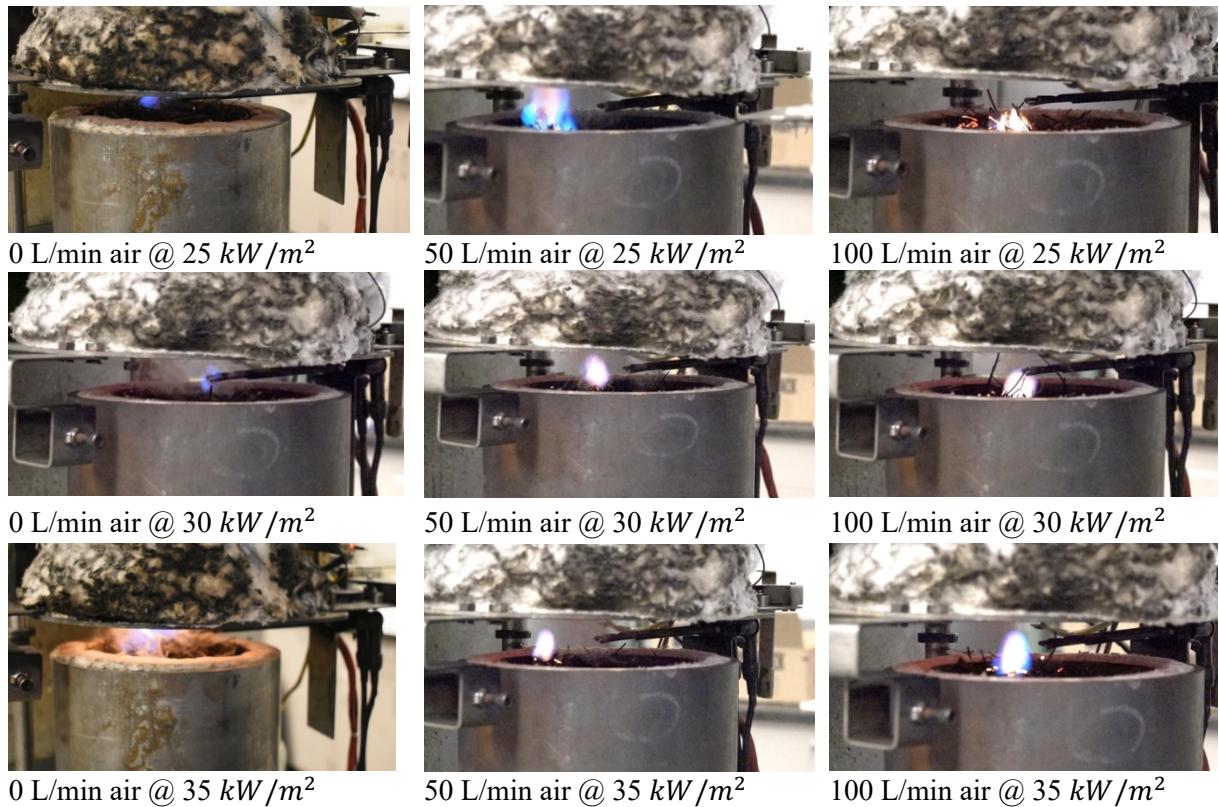


Figure 4.3 Flame location at ignition captured for heat flux ranging from 25 to 35 kW/m² with air flow rates from 0 to 100 L/min.

The most direct observation of the flame position during ignition shows that the type of energy source (spark ignitor and smoldering points) changes with different test conditions, which may reflect the variation of the fuel-oxygen mixture at the spark ignitor with the experimental conditions. The occurrence of smoldering spots before ignition indicates that the fuel vapor generated only by the pyrolysis process is insufficient to support the ignition at the spark ignitor under forced flow conditions, which will be discussed in more detail in sections 4.2.2 to 4.2.4.

4.2.2 Time-to-ignition

Figure 4.4 shows the mean ignition time, t_{ig} measured at external heat fluxes ranging from 20 to 35 kW/m^2 , and airflow rates of 0, 50, and 100 l/min air.

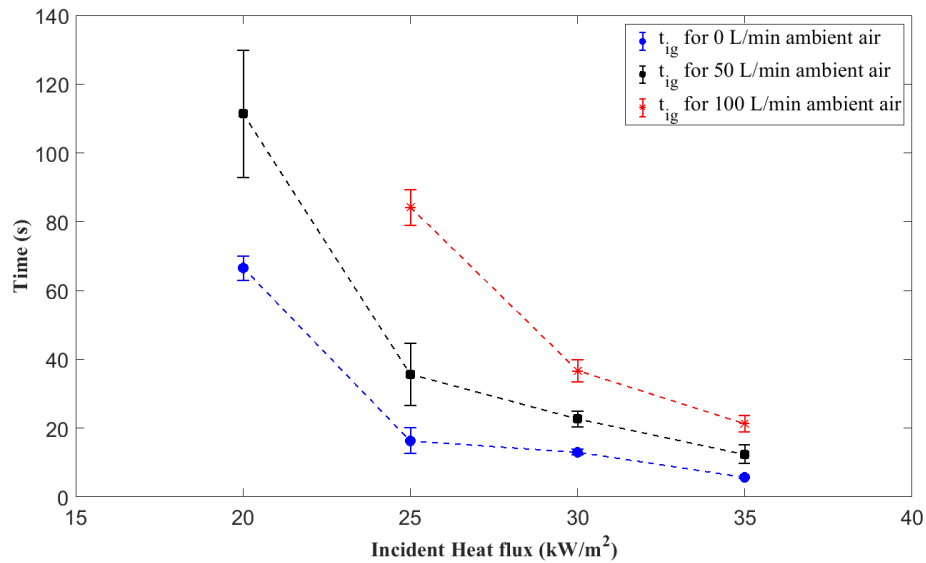


Figure 4.4 Mean ignition time (t_{ig}) for heat flux ranging from 20 to 35 kW/m^2 with air flow rates from 0 to 100 L/min

From the plot, it can be seen that t_{ig} increases when increasing the airflow rate and decreases when increasing the magnitude of the external incident heat flux over the fuel bed. Since t_{ig} can be expressed as the sum of the pyrolysis time for the fuel to achieve pyrolysis temperature and generate sufficient fuel vapor (t_{pyr}), the transport time for the fuel vapor and oxygen to reach the pilot (t_{trans}), and the chemical time for the flammable mixture to proceed to the combustion reaction at the pilot

location (t_{chem}), the variation of t_{ig} on different flow rates and heat fluxes can be analyzed from the variation of t_{pyr} , t_{trans} , and t_{chem} with the different testing conditions.

When increasing the magnitude of the external heat flux over the fuel bed, a greater amount of energy is available to promote the pyrolysis reaction, increasing its rate. Thus, less time is required (which means a decreasing t_{pyr}) until a sufficient fuel rate for ignition is achieved. The generated fuel vapor mixes with the air and transports to the pilot location where the combustion reaction occurs. This transport time (t_{trans}) can be estimated as the ratio of the distance between the fuel bed surface and the spark igniter position to the inflow velocity, as shown in Eq (4.3). When increasing the heat flux, t_{trans} is considered to keep constant with the same rate of inflow applied. Finally, the variation of t_{chem} with heat flux at flaming ignition is negligible, since it is only of the order of 10^{-4} s [11], which is far below the order of magnitude of t_{ig} observed in this work.

$$t_{trans} = \frac{d}{v} \quad \text{Eq (4.3)}$$

where d is the distance between the fuel bed surface and pilot location, taken as 1.3 cm here [12]; and v is the velocity of the pyrolysis gases evolved from the fuel bed.

In short, the decrease in t_{ig} with increasing heat flux is mainly caused by the decreasing t_{pyr} with negligible changes in t_{trans} and t_{chem} .

On the other hand, when increasing the airflow rates, the net heat delivered to the fuel bed decreases due to an enhanced convective cooling through the fuel bed, which cools down the temperature over the fuel bed, thus reduces the pyrolysis reaction rate of the fuel bed and the quantity of the released fuel vapor. Resultantly, it takes longer time for the solid phase to reach the pyrolysis temperature and obtain enough fuel vapor for the flaming ignition. Moreover, the generated fuel vapor through the pyrolysis is diluted in the gas phase by the incoming airflow. Consequently, to achieve at least the lean flammability for the fuel vapor-air mixture in the gas phase which makes the ignition possible, greater amount of fuel vapor needs to be pyrolyzed from the solid phase. Therefore, given an increasing airflow rate, to reach the ignition conditions, more time is needed for the solid phase reaching the pyrolysis

temperature and a greater fuel generation rate (which means an increasing t_{pyr}). The time for transporting the fuel-oxygen mixture to the pilot location (t_{trans}), however, decreases with increasing airflow rates. According to Eq (4.5), t_{trans} is estimated to be 0.27 and 0.14 s for airflow rates of 50 and 100 l/min, respectively. But due to the order of magnitude of t_{ig} , any changes of both t_{trans} and t_{chem} with varying flow rates are negligible. Therefore, the increase in t_{ig} with the increasing airflow rate primarily results from an increase in t_{pyr} .

4.2.3 Mass loss rate per unit area at ignition ($MLRPUA_{ig}$)

The results of mass loss rate per unit area at ignition ($MLRPUA_{ig}$) are shown in Figure 4.5. The uncertainties of the results are determined by one standard deviation of three repetitions for each test.

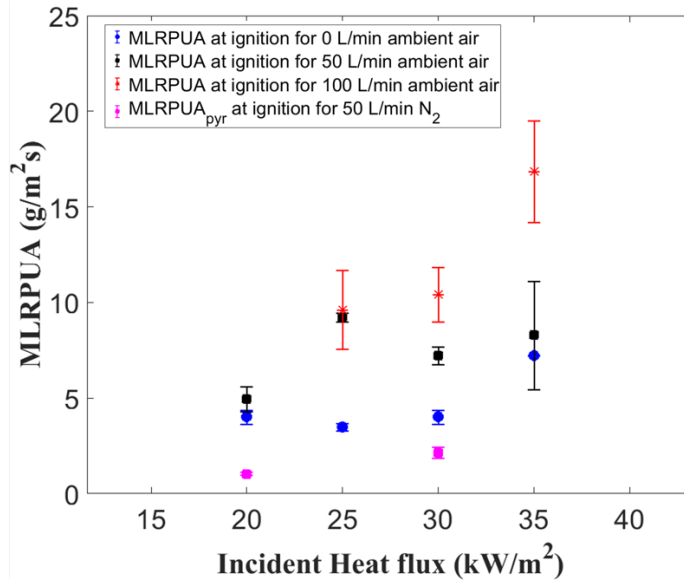


Figure 4.5 Mass loss rate per unit area for sustained flaming ignition ($MLRPUA_{ig}$). $MLRPUA_{pyr}$ was determined by combining the observed time-to-ignition values in the ignition tests with the mass loss rate measured from the pyrolysis tests.

$MLRPUA_{ig}$ was found to increase with both flow rate and external heat flux although the trend of $MLRPUA_{ig}$ with external heat fluxes is less pronounced. This agrees with the trend found by McAllister [13]. Under natural flow conditions, the value of $MLRPUA_{ig}$ is about 3.8 g/m²s for heat fluxes between 20 and 30 kW/m², however, when the heat flux increases to 35 kW/m², $MLRPUA_{ig}$ suddenly increases

from 3.8 to 7.2 g/m²s. In 50 l/min ambient air, $MLRPUA_{ig}$ is about 4.9 g/ m²s at 20 kW/m² and is about 8.2 g/ m²s for heat fluxes between 25 and 35 kW/m². In 100 l/min ambient air, $MLRPUA_{ig}$ is around 10.0 g/ m²s for heat fluxes from 25 to 30 kW/m² and is 16.9 g/ m²s at a heat flux of 35 kW/m².

Two mechanisms mainly drive the mass loss of the fuel bed at ignition. One part of the mass loss is due to pyrolysis while the other one is due to the smoldering combustion of the fuel bed.

When increasing the external incident flux with the same flow condition, the mass loss due to the pyrolysis increases while the mass loss due to the smoldering is likely to be decreased.

Both pyrolysis and smoldering reactions have been found to increase their rate when provided with more energy [14]. Thus, increasing the magnitude of the external incident heat flux over the fuel bed increases the pyrolysis reaction rate, and the smoldering combustion reaction rate. Nevertheless, besides the reaction rate, the thickness of the reaction zone also has an influence on the mass loss for both mechanisms. The pyrolysis thickness of the fuel bed is controlled by radiative heating [15] and convective cooling (if any flow applied) where the depth of radiative heating is mainly a function of fuel volume fraction and surface-to-volume ratio. Namely, the change in thickness for the pyrolysis zone is negligible when increasing the external incident heat flux at the same flow conditions. Consequently, the mass loss due to pyrolysis is to increase with the external incident heat flux. On the other hand, the thickness for the smoldering zone possibly decreases with increasing heat flux due to the fact that fewer smoldering area was observed during the tests. Miller and Bellan [16] also reported a similar trend that the final char yield during biomass pyrolysis decreased with increasing pyrolysis temperature. Thus, it can be assumed that there potentially exists a “best” condition, a balance between the smoldering combustion reaction rate and thickness of the reaction zone that will lead to an extreme mass loss of smoldering combustion for a certain heat flux.

The reason for the increase of $MLRPUA_{ig}$ when increasing the airflow rate is due to the dilution of the flammable mixture. As the chemical reaction at flaming ignition is near stoichiometric [17], the fuel vapor concentration needs to increase with the airflow rates so that the actual equivalence ratio meets

the requirements for ignition. Therefore, to obtain sufficient fuel vapor for ignition, the pyrolysis reaction rate needs to be increased through longer heating time. The pyrolysis reaction rate can also be locally increased by the appearance of smoldering spots, which is consistent with the observation that smoldering was detected before ignition for all tests conducted under forced flow conditions.

4.2.4 Heat release rate per unit area at ignition ($HRRPUA_{ig}$)

The results of the heat release rate per unit area at ignition ($HRRPUA_{ig}$) for sustained ignition are shown in Figure 4.6. The uncertainties of the results are determined by one standard deviation of three repetitions for each test.

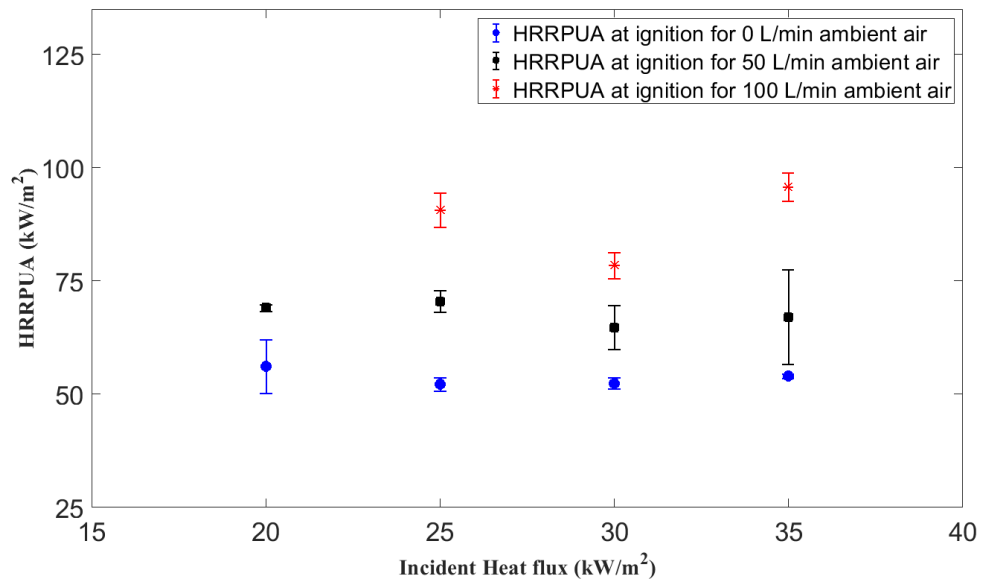


Figure 4.6 Heat Release Rate per unit area at ignition ($HRRPUA_{ig}$) for sustained flaming ignition

The $HRRPUA_{ig}$ increases from 52 kW/m² for a buoyancy-induced flow to 91 kW/m² under a 100 l/min forced ambient airflow. The values measured under natural flow conditions are consistent with those reported by Lyon and Quintiere [17]. The trend of $HRRPUA_{ig}$ under forced flow conditions can be explained by the energy balance for the gas mixture within a control volume near the location of ignition, as shown in Figure 4.7.

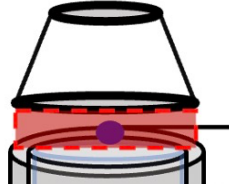


Figure 4.7 Selected control volume (outlined by the red dashed rectangle) for the energy balance analysis at flaming ignition

For sustained flaming ignition, the heat gained from the combustion reaction is sufficient to support a nascent flame while the flame loses heat to the surroundings by convection and radiation. The threshold condition for ignition is the heat provided by the chemical reaction and the ignitor can just balance out the heat losses of the system, as shown in Eq (4.4).

$$\dot{Q}_{ch}'' - h_{total}(T_f - T_{amb}) = 0 \quad \text{Eq (4.4)}$$

Where \dot{Q}_{ch}'' is the energy per unit area provided by chemical reactions happening at ignition; h_{total} is the total heat transfer coefficient of the control volume and equals to the sum of the radiative heat transfer coefficient and the convective heat transfer coefficient, which can be significantly enhanced by increasing flow rates [18]; T_f and T_{amb} are the critical flame temperature below which the flame cannot be sustained, and the ambient temperature respectively.

Solving Eq (4.4) for \dot{Q}_{ch}'' , delivers the following expression that allows for evaluating the minimum chemical energy per unit area required to support the flaming ignition as a function of the participating heat fluxes.

$$\dot{Q}_{ch}'' \text{ (or } HRRPUA_{ig}) = h_{total}(T_f - T_{amb}) \quad \text{Eq (4.5)}$$

Where T_f can be taken as a constant, 1600 K [18].

Therefore, the independency of \dot{Q}_{ch}'' on the external heat fluxes shown in Figure 4.6 is possibly due to the insensitivity to parameters in Eq (4.5) to the heat flux range investigated in this work. On the other hand, the increase in \dot{Q}_{ch}'' when increasing the airflow rates is mainly due to the enhanced convective cooling through the control volume, which leads to an increase in h_{total} .

Furthermore, according to the visual observation that the degree of smoldering is found to be variant with the external heat flux, the contribution of smoldering to the flaming at ignition is to be investigated in this section on the energy level.

Based on what has been discussed in sections 4.2.1 through 4.2.3, the chemical energy released at ignition (\dot{Q}_{ch}) is divided into two parts, as shown in Eq (4.6), to analyze the contribution of smoldering under forced flow conditions.

$$\dot{Q}_{ch} = \dot{Q}_{pyr} + \dot{Q}_{smold} \quad \text{Eq (4.6)}$$

where \dot{Q}_{pyr} and \dot{Q}_{smold} are the energy released by the combustion of pyrolysis gas, and smoldering.

Combining the results from pyrolysis tests, \dot{Q}_{pyr} is able to be calculated based on Eq (4.7), where \dot{m}_{pyr} is the mass loss rate due to pyrolysis; H_{c_pyr} is the heat of combustion for the pyrolysis gas.

$$\dot{Q}_{pyr} = \dot{m}_{pyr} \cdot H_{c_pyr} \quad \text{Eq (4.7)}$$

Figure 4.8 shows the mass loss rate evolution for pyrolysis and ignition tests conducted with the air or nitrogen flow rate of 50 l/min, under incident heat flux of 20, 30 kW/m^2 . From the plots, it is reasonable to consider the mass loss due to pyrolysis at flaming ignition (\dot{m}_{pyr}) equals the total mass loss rate (MLR) just before the glowing starts. The implicit assumption is that smoldering does not interact with pyrolysis. Therefore, the values of \dot{m}_{pyr} under 20, 30 kW/m^2 incident heat flux and 50 l/min O_2 are respectively 0.009 and 0.024 g/s. Accordingly, as another part of the mass loss at ignition, the values of \dot{m}_{smold} under 20, 30 kW/m^2 and 50 l/min O_2 are respectively 0.069 and 0.081 g/s. Based on the values obtained from the pyrolysis tests, the heat of combustion for the generated pyrolysis gas (H_{c_pyr}) are 2.6 and 6.4 kJ/g for incident heat flux of 20 and 30 kW/m^2 , respectively.

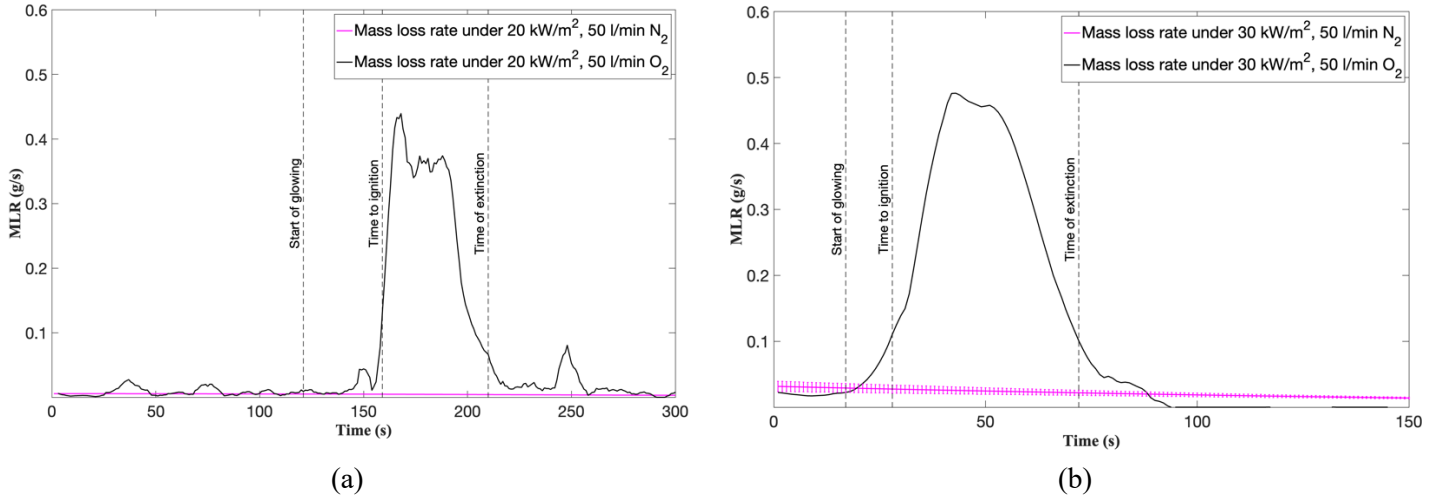


Figure 4.8 Mass loss rate evolution (MLR) for tests conducted with (a) 20 kW/m^2 , 50 l/min N_2 and O_2 , and (b) 30 kW/m^2 , 50 l/min N_2 and O_2

Substituting the values of \dot{m}_{pyr} and H_{c_pyr} into Eq (4.7), the contribution of pyrolysis gas at ignition, \dot{Q}_{pyr} in Table 4.3, is quantified while the energy provided by smoldering at ignition can be determined based on Eq (4.6) by combing the computed \dot{Q}_{pyr} and \dot{Q}_{ch} obtained from experiment measurements. The results presented in Table 4.3 show that energy provided by smoldering combustion (\dot{Q}_{smold}) under 50 l/min ambient air is the dominant contribution to the ignition. When increasing the external heat flux from 20 to 30 kW/m^2 given the same flow rate, the percentages of smoldering to the total chemical energy drops from 98.47% to 81.84% due to the increasing reaction rate and flammability of the pyrolysis gas. Therefore, the contribution of smoldering combustion to the ignition decreases with increasing external incident heat flux, which is consistent with the fact that less smoldering was observed for higher heat flux.

Table 4.3 Energy provided to the ignition by pyrolysis gas combustion and smoldering combustion for 20 and 30 kW/m^2 under 50 l/min ambient air

Heat flux (kW/m^2)	\dot{m}_{pyr} (g/s)	H_{c_pyr} (kJ/g)	\dot{Q}_{pyr} (kW)	\dot{Q}_{ch} (kW)	\dot{Q}_{smold} (kW)	$(\dot{Q}_{smold}/\dot{Q}_{ch})$ (%)
20	0.005	2.60	0.013	0.848	0.835	98.47
30	0.024	6.42	0.154		0.694	81.84

4.3 References

- [1] E. Granada, P. Eguía, J. A. Vilan, J. A. Comesaña, and R. Comesaña, “FTIR quantitative analysis technique for gases. Application in a biomass thermochemical process,” *Renewable Energy*, vol. 41, pp. 416–421, May 2012, doi: 10.1016/j.renene.2011.11.020.
- [2] E. Amini, M. S. Safdari, J. T. DeYoung, D. R. Weise, and T. H. Fletcher, “Characterization of pyrolysis products from slow pyrolysis of live and dead vegetation native to the southern United States,” *Fuel*, vol. 235, pp. 1475–1491, Jan. 2019, doi: 10.1016/j.fuel.2018.08.112.
- [3] P. Fu, W. Yi, X. Bai, Z. Li, S. Hu, and J. Xiang, “Effect of temperature on gas composition and char structural features of pyrolyzed agricultural residues,” *Bioresource Technology*, vol. 102, no. 17, pp. 8211–8219, Sep. 2011, doi: 10.1016/j.biortech.2011.05.083.
- [4] M. el Houssami et al., “Experimental and numerical studies characterizing the burning dynamics of wildland fuels,” *Combust Flame*, vol. 168, pp. 113–126, Jun. 2016, doi: 10.1016/j.combustflame.2016.04.004.
- [5] N. Wright, D. Osborne, and N. Music, “Comparison of hydrocarbon measurement with FTIR and FID in a dual fuel locomotive engine,” in SAE technical papers, Apr. 2016, vol. 2016-April, no. April. doi: 10.4271/2016-01-0978.
- [6] G. Ningbo, L. Baoling, L. Aimin, and L. Juanjuan, “Continuous pyrolysis of pine sawdust at different pyrolysis temperatures and solid residence times,” *Journal of Analytical and Applied Pyrolysis*, vol. 114, pp. 155–162, Jul. 2015, doi: 10.1016/j.jaap.2015.05.011.
- [7] M. I. Jahirul, M. G. Rasul, A. A. Chowdhury, and N. Ashwath, “Biofuels production through biomass pyrolysis- A technological review,” *Energies*, vol. 5, no. 12. MDPI AG, pp. 4952–5001, 2012. doi: 10.3390/en5124952.
- [8] N. Kiggundu and J. Sittamukyoto, “Pyrolysis of Coffee Husks for Biochar Production,” *J Environ Prot (Irvine, Calif)*, vol. 10, no. 12, pp. 1553–1564, 2019, doi: 10.4236/jep.2019.1012092.
- [9] J. G. Quintiere, *Fundamentals of fire phenomena*. John Wiley, 2006.
- [10] D. Cancellieri, E. Leoni, and J. L. Rossi, “Kinetics of the thermal degradation of Erica arborea by DSC: Hybrid kinetic method,” *Thermochim Acta*, vol. 438, no. 1–2, pp. 41–50, Nov. 2005, doi: 10.1016/j.tca.2005.07.013.
- [11] S.R. Turns, *An introduction to combustion*, 3rd edition. McGraw Hill. 2011.
- [12] 2017, ASTM E1354: Standard test method for heat and visible smoke release rates for materials and products using an oxygen consumption calorimeter.
- [13] S. McAllister, “Critical mass flux for flaming ignition of wet wood,” *Fire Safety Journal*, vol. 61, pp. 200–206, 2013, doi: 10.1016/j.firesaf.2013.09.002.
- [14] A. Bartlett and L. A. Bisby, “Analysis of cross-laminated timber upon exposure to non-standard heating,” *Fire and Materials*. 2015. <https://www.researchgate.net/publication/270875737>
- [15] Thomas, J.C., Everett, J., Simeoni, A., Skowronski, N.S., & Torero, J.L. (2013). *Flammability Study of Pine Needle Beds*.
- [16] R. S. Miller and J. Bellan, “A generalized biomass pyrolysis model based on superimposed cellulose, hemicellulose and lignin kinetics,” *Combustion Science and Technology*, vol. 126, no. 1–6, pp. 97–137, 1997, doi: 10.1080/00102209708935670
- [17] R. E. Lyon and J. G. Quintiere, “Criteria for piloted ignition of combustible solids,” *Combustion and Flame*, vol. 151, no. 4, pp. 551–559, Dec. 2007, doi: 10.1016/j.combustflame.2007.07.020.
- [18] Kosky, P., Balmer, R.T., Keat, W.T., & Wise, G. *Exploring Engineering*. Academic Press. 2011.

Chapter 5 CONCLUSION AND FUTURE WORK

5.1 Conclusion

Two types of tests were conducted to investigate the pyrolysis process and the ignition behavior of *Pinus palustris* needle beds.

In the pyrolysis tests, the influence of different heat fluxes on the pyrolysis gas composition was investigated. The primary components of pyrolysis gas were found to be CH₄, CO, CO₂, and H₂O. The composition of the pyrolysis gas was not affected by the experimental conditions. However, the percentage of these components was found to vary with the magnitude of the external incident heat flux. The results showed that (1) the pyrolysis reaction rate increases when increasing the external incident heat flux over the fuel surface, and (2) the pyrolysis gas is of greater heat of combustion at a higher external heat flux.

In the ignition tests, the influence of the external heat flux and air flow rate on the time to ignition, the mass loss rate, and the heat release rate at ignition was analyzed. The analysis of the time-to-ignition results indicated that decreasing heat fluxes and increasing airflow rates extend the ignition time mainly by extending the pyrolysis time. The analysis of the mass loss rate and the heat release rate at ignition suggest significant contributions of smoldering combustion to flaming ignition under low heat fluxes and high airflow rate conditions. In addition, the degree of smoldering at ignition on a bench scale can be indirectly evaluated by quantifying the chemical energy released by the combustion of pyrolysis gas.

5.2 Future work

For the pyrolysis tests, further experiments should be conducted with broader ranges of incident heat flux levels and flow rates in atmospheres of both pure nitrogen and the mixture of nitrogen and oxygen. The focus is to investigate (1) the influence of irradiance level on the reaction rate, and the heat of combustion of the pyrolysis gas; (2) the role of diffusion on the pyrolysis rate and the heat of combustion of the pyrolysis gas; and (3) the influence of oxygen presence on the pyrolysis rate and the heat of combustion for the pyrolysis gas.

It is worth noting that technical issue may arise for the pyrolysis tests conducted under higher inflow rates when the FTIR spectroscopy is applied to analyze the pyrolysis gas. This is due to the difficulty of dynamically capturing pyrolysis gases at high inflow rates (“short “residence time) while maintaining sufficient instrument resolution (“long” scan time) to ensure that pyrolytic compounds can be detected.

For the ignition tests, the focus should be using a wider range of incident heat flux and flow conditions to investigate (1) the influence of flow on the ignition time in terms of cooling and mixing (oxygen supply) effect with varying external incident heat flux; (2) the influence of external heat flux and flow on the mass loss due to pyrolysis as well as smoldering; and (3) the relationship between the heat of combustion for the pyrolysis gas and the contribution of smoldering combustion by combining the pyrolysis test results.

Appendix A UNCERTAINTY ANALYSIS OF HEAT OF COMBUSTION EVALUATION

Estimates of uncertainty are evaluated using the method described by Taylor and Kuyatt [A.1]. A series of measurements, denoted by y , can be expressed as a function (f) of its associated independent variables, x_i , as shown in Eq (A.1)

$$y = f(x_1, x_2, x_3, \dots, x_n) \quad \text{Eq (A.1)}$$

In the case that all input parameters are uncorrelated, the combined uncertainty is given by Eq (A.2), referred to as the law of propagation of uncertainty (also called as “root-sum-of-squares”).

$$u_c(y) = \sqrt{\sum_{i=1}^n \left(\frac{\partial f}{\partial x_i} \cdot u(x_i) \right)^2} \quad \text{Eq (A.2)}$$

where $u_c(y)$ is the combined uncertainty; $u(x_i)$ is the uncertainty of each input parameter and determined by one standard deviation.

Therefore, combining the Eqs (A.2) and (4.1), the uncertainty of computed heat of combustion (See section 4.1, chapter 4) can be expressed below as Eq (A.3) and, consequently, Eq (A.4). The results for the uncertainty evaluation of pyrolysis gas heat of combustion are presented in Table A1.

$$H_{c_pyr} = Y_{CO} \cdot H_{c_CO} + Y_{CH_4} \cdot H_{c_CH_4} \quad \text{Eq (4.1)}$$

$$u_c(H_{c_pyr}) = \sqrt{\left(\frac{\partial H_{c_pyr}}{\partial Y_{CO}} \cdot u(Y_{CO}) \right)^2 + \left(\frac{\partial H_{c_pyr}}{\partial Y_{CH_4}} \cdot u(Y_{CH_4}) \right)^2} \quad \text{Eq (A.3)}$$

$$u_c(H_{c_pyr}) = \sqrt{\left(H_{c_CO} \cdot u(Y_{CO}) \right)^2 + \left(H_{c_CH_4} \cdot u(Y_{CH_4}) \right)^2} \quad \text{Eq (A.4)}$$

Table A1. Uncertainty analysis of evaluated heat of combustion for the pyrolysis gas

Heat flux (kW/m ²)	Y_{CH_4}	$u(Y_{CH_4})$	$H_{c_CH_4}$ (kJ/g)	Y_{CO}	$u(Y_{CO})$	H_{c_pyr} (kJ/g)	H_{c_pyr} (kJ/g)	$u(H_{c_pyr})$ (kJ/g)
20	0.043	0.02	50.1	0.11	0.02	10.1	2.6	0.14
30	0.085	0.01		0.21	0.02		6.4	0.12

[A.1] B. N. Taylor and C. E. Kuyatt, "Guidelines for evaluating and expressing the uncertainty of NIST measurement results," 1994.